Draft version February 2, 2008
Preprint typeset using LaTeX style emulateapj v. 6/22/04

arXiv:astro-ph/0501229v1 12 Jan 2005

APERTURE EFFECTS ON STAR FORMATION RATE, METALLICITY AND REDDENING

Lisa J. Kewley[1]
Harvard-Smithsonian Center for Astrophysics and
60 Garden Street MS-20, Cambridge, MA 02138

Rolf A. Jansen
Dept. of Physics & Astronomy, Arizona State University and
P.O. Box 871504, Tempe, AZ 85287-1504

Margaret J. Geller
Smithsonian Astrophysical Observatory and
60 Garden Street MS-20, Cambridge, MA 02138

Draft version February 2, 2008

ABSTRACT

We use 101 galaxies selected from the Nearby Field Galaxy Survey (NFGS) to investigate the effect of aperture size on the star formation rate, metallicity and reddening determinations for galaxies. Our sample includes galaxies of all Hubble types except ellipticals with global SFRs ranging from 0.01 to 100 $\mathrm{M}_{\odot}\mathrm{yr}^{-1}$, metallicities between $7.9 \lesssim \log(\mathrm{O/H})+12 \lesssim 9.0$, and reddening between $0 \lesssim A(V) \lesssim 3.3$. We compare the star formation rate, metallicity and reddening derived from nuclear spectra to those derived from integrated spectra. For apertures capturing $< 20\%$ of the B_{26} light, the differences between nuclear and global metallicity, extinction and star formation rate are substantial. Late-type spiral galaxies show the largest systematic difference of ~ 0.14 dex in the sense that nuclear metallicities are greater than the global metallicities. Sdm, Im, and Peculiar types have the largest scatter in nuclear/integrated metallicities, indicating a large range in metallicity gradients for these galaxy types or clumpy metallicity distributions. We find little evidence for systematic differences between nuclear and global extinction estimates for any galaxy type. However, there is significant scatter between the nuclear and integrated extinction estimates for nuclear apertures containing $< 20\%$ of the B_{26} flux. We calculate an 'expected' star formation rate using our nuclear spectra and apply the commonly-used aperture correction method. The expected star formation rate overestimates the global value for early type spirals, with large scatter for all Hubble types, particularly late types. The differences between the expected and global star formation rates probably result from the assumption that the distributions of the emission-line gas and the continuum are identical. The largest scatter (error) in the estimated SFR occurs when the aperture captures $< 20\%$ of the B_{26} emission. We discuss the implications of these results for metallicity-luminosity relations and star-formation history studies based on fiber spectra. To reduce systematic and random errors from aperture effects, we recommend selecting samples with fibers that capture $> 20\%$ of the galaxy light. For the Sloan Digital Sky Survey and the 2dFGRS, redshifts $z > 0.04$ and $z > 0.06$ are required, respectively, to ensure a covering fraction $> 20\%$ for galaxy sizes similar to the average size, type, and luminosity observed in our sample. Higher-luminosity samples and samples containing many late-type galaxies require a larger minimum redshift to ensure that $> 20\%$ of the galaxy light is enclosed by the fiber.

Subject headings: galaxies: starburst—galaxies: abundances—galaxies: fundamental parameters—galaxies: spiral—techniques: spectroscopic

1. INTRODUCTION

Unprecedented insight into galaxy evolution has recently been obtained with very large spectroscopic surveys, including the Sloan Digital Sky Survey (SDSS) and the 2 degree Field Galaxy Redshift Survey (2dFGRS). These spectroscopic surveys allow fundamental physical properties of galaxies to be studied with increasingly large datasets. Galaxy star formation rates and the metallicity-luminosity relation can now be analysed as a function of redshift for samples containing thousands of galaxies (e.g., Baldry et al. 2002; Nakamura et al. 2003; Schulte-Ladbeck et al. 2004; Lamareille et al. 2004; Tremonti et al. 2004).

Unfortunately, comparisons of the spectroscopic properties of nearby galaxies with those at higher redshifts can be severely hindered by aperture effects. The combination of a fixed-size aperture and radial gradients and variations in metallicity, star-formation, and extinction can lead to a bias in these properties that may mimic or hide evolution as a function of redshift. Typical fiber diameters are 3″ for the SDSS and 2″ for the 2dFGRS. Spectra of nearby galaxies taken through such small apertures cover only a small portion of the nearest galaxies and capture a small fraction of their integrated light.

Early studies of the effect of aperture size on apparent galaxy properties were carried out decades ago.

Electronic address: lkewley@cfa.harvard.edu
[1] CfA Fellow

de Vaucouleurs (1961) and Hodge (1963) used various aperture sizes to show that early-type galaxies are redder in their galaxy centers. Tinsley (1971) pointed out that the color-aperture relation seen in early-type spiral galaxies leads to the observation of bluer colors at higher-z in an aperture of small fixed angular size.

Recent investigations into aperture effects have focused on spectral classification and star formation rates. Zaritsky, Zabludoff, & Willick (1995) showed that galaxies in the Las Campanas Redshift Survey (LCRS) at redshifts $z < 0.05$ may be misclassified because the $3.5''$ fibers capture only the central fraction of the galaxies' light.

The Hα emission-line is commonly used to estimate star-formation rates in galaxies with redshifts $z < 0.3$. Pérez-González et al. (2003) analysed the Hα emission in a sample of local star-forming galaxies selected from the Universidad Complutense de Madrid (UCM) Survey. Pérez-González et al. concluded that long-slit or fiber spectra of nearby galaxies can miss substantial fractions of the emission-line flux (typically 50-70%). They suggest supplementing emission-line fluxes with direct emission-line imaging to overcome this bias. However, for large samples covering a range of redshifts, Hα imaging of every galaxy is not currently viable.

Flux calibration of spectra in fiber-based surveys is difficult. Thus Hα emission-line equivalent widths (EWs) are often used along with an $r-$band magnitude to estimate star formation rates. Gómez et al. (2003) pointed out that aperture bias may result in a systematic increase in the observed Hα equivalent width (EW) for higher redshift galaxies relative to lower redshift galaxies in the SDSS. Gomez et al. analysed SDSS galaxies within three equal volume redshift bins between $0.05 < z < 0.095$. They found no evidence for an increase in the median and 75th percentile of the Hα EW distribution among these three bins.

Hopkins et al. (2003) investigated aperture effects on Hα-based star-formation rates in the SDSS by comparing the Hα SFRs with those derived from the radio. They found that the Hα SFRs are overestimated for galaxies requiring the largest aperture corrections. The galaxies requiring the largest aperture corrections are either the closest or the most massive galaxies. Because of the large scatter between the two SFRs, Hopkins et al. were unable to quantify this aperture effect.

The effect of aperture on metallicity, extinction, and star formation rate has been difficult to quantify without high quality nuclear and global spectra for galaxies spanning a broad range in Hubble type. In this paper, we use the Nearby Field Galaxy Survey (NFGS; Jansen et al. 2000a,b) to investigate aperture effects on star-formation rate, metallicity, and extinction. The NFGS is ideal for an aperture effect investigation because it provides integrated and nuclear spectra for 198 objectively selected nearby galaxies. The NFGS (described in Section 2) spans the full range in Hubble type and absolute magnitude in the CfA redshift catalog, thus enabling an investigation into aperture effects as a function of both galaxy type and luminosity. In Section 3, we investigate and quantify the flux coverage of our nuclear and integrated spectral apertures. In Section 4, we investigate the effect of aperture on metallicity estimates. We show the effect of aperture on extinction estimates in Section 5, and we study the effect of aperture on star-formation rates in Section 6. In each section we discuss the implications of our results in terms of the SDSS and 2dFGRS fiber-based sky surveys and their current aperture-correction methods. In Section 8, we conclude that a minimum flux covering fraction of $\gtrsim 20\%$ is required for reliable estimates of extinction, metallicity and star formation rate, for samples with a similar mean galaxy size to that of the NFGS. Throughout this paper, we adopt the flat Λ-dominated cosmology as measured by the WMAP experiment ($h = 0.72$, $\Omega_m = 0.29$; Spergel et al. 2003).

2. SAMPLE SELECTION AND SPECTROPHOTOMETRY

The NFGS is ideal for investigating aperture effects in galaxies because it is an objectively selected (unbiased) sample with both integrated and nuclear spectra. Jansen et al. (2000a) selected the NFGS sample by sorting the CfA1 redshift survey (Davis & Peebles 1983; Huchra et al. 1983) into 1 mag-wide bins of M_Z. Within each bin, the sample was sorted according to CfA1 morphological type. To avoid a strict diameter limit, which might introduce a bias against the inclusion of low surface brightness galaxies in the sample, Jansen et al. imposed a radial velocity limit, $\mathrm{V_{LG}(km\,s^{-1})} > 10^{-0.19-0.2\mathrm{M_z}}$ (with respect to the Local Group standard of rest). Galaxies in the direction of the Virgo Cluster were excluded to avoid a sampling bias favoring a cluster population. Lastly, every *Nth* galaxy in each bin was selected to approximate the local galaxy luminosity function (e.g., Marzke, Huchra, & Geller 1994). The final 198-galaxy sample contains the full range in Hubble type and absolute magnitude present in the CfA1 galaxy survey and is a fair representation of the local galaxy population.

Jansen et al. (2000b) provide integrated and nuclear spectrophotometry for almost all galaxies in the NFGS sample. They obtained integrated spectra by scanning a $3''$ slit across each galaxy. The resulting integrated spectra include 52-97% of the light enclosed within the B_{26} isophote, with an average B_{26} fraction of 82±7% for the 198 galaxy NFGS sample. These spectra represent the luminosity weighted mean of the emission from stars and H II regions over a wide range in distance from the galaxy center.The integrated emission-line properties are therefore weighted towards the highest surface brightness, largest, and least extincted H II regions.

The nuclear spectra were obtained with a $3''$ slit centered on the nucleus and aligned along the major axis of each galaxy, sampling $3'' \times 6.''84$. The covering fraction of the nuclear spectra depends on the radial light profile and ranges between 0.4-72% of the light within the B_{26} isophote, with an average covering fraction of 10±11%.

We have calibrated the integrated and nuclear fluxes to absolute fluxes by careful comparison with B-band surface photometry (described in Kewley et al. 2002, ; hereafter Paper I). We corrected the Hα and Hβ emission-line fluxes for underlying stellar absorption as described in Paper I.

We used two methods to correct the NFGS emission-line fluxes for Galactic extinction, based on: (1) the HI maps of Burnstein & Heiles (1984), as listed in the Third Reference Catalogue of Bright Galaxies (de Vaucouleurs et al. 1991), and (2) the COBE and IRAS maps (plus the Leiden-Dwingeloo maps of HI emission) of Schlegel, Finkbeiner & Davis (1998). The average Galactic extinction is $E(B-V)$=0.014 $\pm$ 0.003 (method 1) or $E(B-V)$=0.016 $\pm$ 0.003 (method 2).

To reject galaxies with significant emission from an AGN, we used the nuclear and integrated optical emission-line ratios to classify the galaxies. For those galaxies with [O III]/Hβ, [N II]/Hα, and (if available) [S II]/Hα ratios, we used the theoretical optical classification scheme developed by Kewley et al. (2001a). In this scheme, galaxies that lie above the theoretical "extreme starburst line" in the standard optical diagnostic diagrams are classed as AGN, while those that lie below the line are classed as HII region-like. Galaxies that lie in the AGN region in one diagnostic diagram but in the HII region section of the other diagram are classed as "ambiguous" (AMB) galaxies. A fraction of galaxies in the NFGS (35/198) have [N II]/Hα ratios but immeasurable [O III] or Hβ fluxes in their nuclear (24/198) and/or integrated (15/198) spectra. These galaxies are classified as HII region-like if log([N II]/Hα)< -0.3, typical of starburst galaxies and HII regions (e.g., Kewley et al. 2001b; Dopita et al. 2000). We are unable to classify those galaxies with $-0.3 \leq$log([N II]/Hα)$\leq$ 0.0 if [O III]/Hβ is unavailable because such line ratios can be produced by both AGN and starburst galaxies. Galaxies without [O III]/Hβ but with strong log([N II]/Hα)$>$ 0.0 are classed as AGN (e.g., Figure 1 of Brinchmann et al. 2004). Our final adopted classification is based on the nuclear class if available and the integrated class otherwise. We provide the global, nuclear, and adopted classes for the NFGS sample in Table 1. We give quality flags, Q, for the global and nuclear classes based on the number of line ratios used for classification. Quality flags Q =1, 2, and 3 correspond to the use of {[O III]/Hβ, [N II]/Hα, [S II]/Hα}, {[O III]/Hβ, [N II]/Hα}, and [N II]/Hα respectively. Following this scheme, the emission-line ratios indicate that the global spectra of 118/198 NFGS galaxies are dominated by star formation, 12/198 are dominated by AGN, and 8/198 are "ambiguous" galaxies. The remaining galaxies do not have sufficient emission-lines in their spectra to allow classification. Many of these unclassified galaxies are ellipticals. Because ambiguous galaxies are likely to contain both starburst and AGN activity (see e.g., Kewley et al. 2001b; Hill et al. 1999), we do not include them in the following analysis.

We note that the fraction of AGN found in surveys may depend on the aperture size. Larger apertures may include more emission from extra-nuclear HII regions, changing the classification from AGN to HII region-like (Storchi-Bergmann 1991). The NFGS does not contain a sufficiently large number of galaxies with significant AGN activity to investigate the effect of aperture on classification quantitatively. Of the 115 NFGS galaxies with both nuclear and global classifications, 2 galaxies change class from their integrated to nuclear spectra; A0857+5242 changes from HII region-like to an AGN class, and NGC 3165 changes from HII region-like to ambiguous. It is not possible to investigate a variation in nuclear to integrated [N II]/Hα, [O III]/Hβ, or [S II]/Hα ratios in terms of a potential AGN contribution because variations in these ratios are likely to be driven by gradients in metallicity ([N II]/Hα, [O III]/Hβ) and/or ionization parameter ([N II]/Hα, [O III]/Hβ, [S II]/Hα) in HII region-like galaxies (e.g., Kewley et al. 2001a).

To calculate the extinction and star formation rates, we require measurable Hα and Hβ emission-line fluxes. We calculate metallicities using the Kewley & Dopita (2002) "recommended" method. To utilize this method, we also require [O II]λ3727 and [N II]λ6584 fluxes for log([N II]/[O II])$\gtrsim -1.0$. For log([N II]/[O II])$\lesssim -1.0$, we require measureable [O II]λ3727 and [O III]$\lambda\lambda$4959, 5007. A total of 101/118 HII region-like galaxies in the NFGS satisfy these criteria. These 101 galaxies (Table 2) constitute the sample we analyse here.

Because of low S/N ratios in the [O III]λ4959 emission-line, we used the theoretical ratio [O III]λ5007/[O III]λ4959 $\sim$ 3 to calculate the [O III]λ4959 flux. Errors in the absolute metallicities are $\sim$ 0.1 in log(O/H)+12 units (see Kewley & Dopita 2002, for a discussion). These errors primarily reflect the accuracy of the theoretical models used to create the metallicity diagnostics. Any error introduced by the diagnostics is likely to be systematic (e.g., Kobulnicky & Kewley 2004). Because we are using *the same* metallicity diagnostic for both nuclear and integrated spectra, errors in the *relative* metallicities should be $\ll$ 0.1 dex.

We corrected the emission line fluxes for reddening using the Balmer decrement and the Cardelli, Clayton, &Mathis (1989) (CCM) reddening curve. We assumed an $\mathrm{R_V = A_V/E(B-V)}$ = 3.1 and an intrinsic Hα/Hβ ratio of 2.85 (the Balmer decrement for case B recombination at T= 10^4K and $n_e \sim 10^2 - 10^4 \mathrm{cm}^{-3}$; Osterbrock 1989). After removing underlying Balmer absorption, 6/101 galaxies have Hα/Hβ $<$ 2.85 for both integrated and nuclear spectra, 11/101 galaxies have Hα/Hβ $<$ 2.85 for nuclear spectra and Hα/Hβ $>$ 2.85 for integrated spectra, and 3/101 galaxies have Hα/Hβ $<$ 2.85 for integrated spectra and Hα/Hβ $>$ 2.85 for nuclear spectra. A Balmer decrement $<$ 2.85 results from a combination of: (1) intrinsically low reddening, (2) errors in the stellar absorption correction, and (3) errors in the line flux calibration and measurement. Errors in the stellar absorption correction and flux calibration are discussed in detail in Paper I, and are ~12-17% on average, with a maximum error of $\sim$ 30%. For the S/N of our data, the lowest E(B-V) measurable is 0.02. We therefore assign these galaxies an upper limit of E(B-V)$<$ 0.02. The difference between applying a reddening correction with an E(B-V) of 0.02 and 0.00 is minimal: an E(B-V) of 0.02 corresponds to an attenuation factor of 1.04 at Hα using the CCM curve.

3. FLUX COVERAGE

3.1. *Reference flux: B_{26} isophote*

For our analysis, we define flux coverage in terms of the flux contained within the directly observed B_{26} isophote. Because we are investigating the emission-line properties of the NFGS galaxies, we assume that the majority of the emission-line gas is contained within the B_{26} isophote. This assumption could potentially introduce selection effects into our analysis if the flux contained within the B_{26} isophote differs systematically from the total B-band flux as a function of galaxy type or luminosity. Figure 1 compares the fraction of B_{26} light captured within our integrated spectral aperture, $I_{int}/I_{B_{26}}$, with

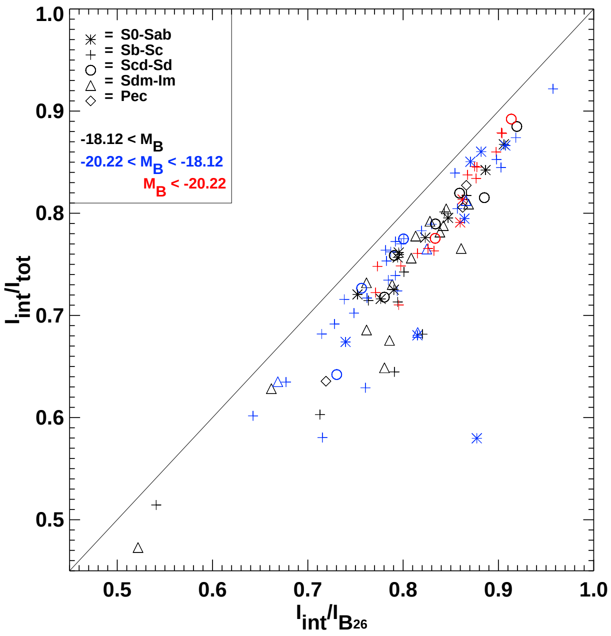

FIG. 1.— Integrated light as a fraction of the B_{26} isophotal light ($I_{int}/I_{B_{26}}$) versus the integrated light as a fraction of the total B-band light (I_{int}/I_{tot}). Symbols and colors give the Hubble type and luminosity range shown in the legend. We assume $M_* = -20.22$ (Marzke et al. 1998, after conversion to our adopted cosmology) . The solid y=x line shows where the data would lie if $I_{B_{26}}$ is representative of the total B-band flux. The mean offset from the y=x line is 0.039 ± 0.003. The majority ($72/82 \sim 88\%$) of the galaxies have a mean offset close to 0.039, regardless of luminosity. The light contained within the B26 isophote provides a well-defined and largely unbiased proxy for the total flux.

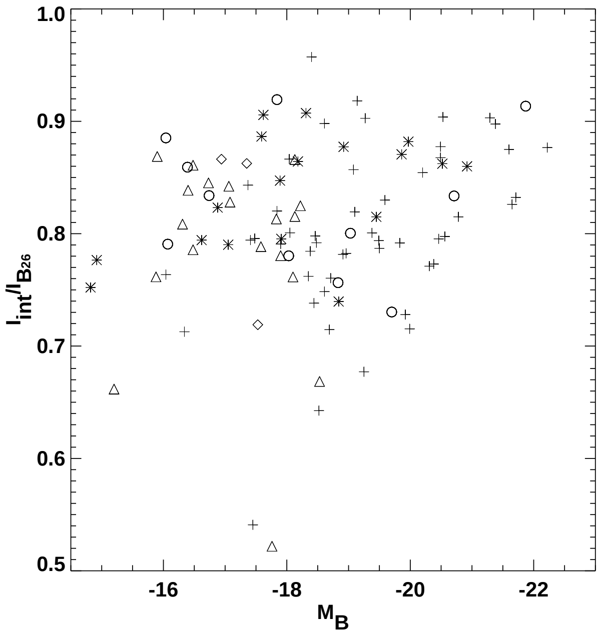

FIG. 2.— The fraction of B_{26} light captured within our integrated spectral aperture compared with the blue absolute magnitude, M_B. Symbols are the same as in Figure 1. Excluding the 6 galaxies with $\mathrm{I_{int}/I_{B_{26}}} < 0.7$, we find no significant dependence of the integrated $\mathrm{B_{26}}$ fraction on absolute magnitude.

the fraction of extrapolated total B-band light, I_{tot}, captured within our integrated spectral aperture, I_{int}/I_{tot}. The solid y=x line shows where the data would lie if the B_{26} flux represented 100% of the B-band total flux. The mean deviation of our data from the y=x line is 0.039 ± 0.003. A small fraction of galaxies (10/101) deviate from the y=x line by more than 0.07. These 10 galaxies include 2 early-type spirals (S0-Sab), 5 late-type spirals (Sb–Sd) and 3 very late-types (Sdm–Im–Pec). Therefore, the use of the B_{26} flux as a reference should not introduce a bias as a function of galaxy type. The galaxies in Figure 1 are color-coded according to their B-band Magnitude. We assume $M_* = -20.22$ (Marzke et al. 1998, ; after conversion to our adopted cosmology). The 10 outlying galaxies fall in the lower two luminosity bins ($M_B > -20.22$; black and blue symbols). However the majority ($72/82 \sim 88\%$) of the galaxies with $M_B > -20.22$ display a similar deviation from the y=x line than the $M_B < -20.22$ galaxies (red symbols). We conclude that the use of the B_{26} flux as a reference should not introduce a significant bias as a function of luminosity.

In Figure 2, we compare the fraction of B_{26} light captured within our integrated spectral aperture ($I_{int}/I_{B_{26}}$) with the blue absolute magnitude. The Spearman Rank test gives a correlation coefficient of -0.19. The probability of obtaining this value by chance is 6%, indicating that $I_{int}/I_{B_{26}}$ is correlated (albeit weakly) with M_B. Robust correlation methods give similar correlation coefficients; both the Biweight Midcovariance method and Pearson's Product Moment Correlation give correlation coefficients of -0.22. This correlation is driven by the 6/101 galaxies with $I_{int}/I_{B_{26}} < 0.7$ and the 7/101 galaxies more luminous than $M_B = -21$. Excluding these 13 galaxies gives a correlation coefficient of -0.05, with a probability of obtaining this value by chance of 66%. The integrated spectral properties of the 6 galaxies with $I_{int}/I_{B_{26}} < 0.7$ may not be representative of their global properties. We therefore mark these galaxies with a large circle in the Figures in the subsequent sections.

In Figure 3 we compare $I_{int}/I_{B_{26}}$ with the B-band central surface brightness, μ_0^B. Not surprisingly, the integrated spectral aperture includes a larger portion of the B_{26} light for brighter galaxies. The Spearman Rank, Pearson's Product Moment, and the Biweight Midsector tests indicate that $I_{int}/I_{B_{26}}$ is correlated with μ_0^B; the correlation coefficient is -0.36, -0.36, -0.34 respectively (the probability of obtaining this value by chance is 0.03%). This correlation is partly driven by the 6 galaxies with $I_{int}/I_{B_{26}} < 0.7$ and the 12 galaxies with $\mu_0^B < -19.5$. Removing these 17 galaxies does not entirely remove this correlation; a weak correlation remains with a correlation coefficient of -0.17, -0.13, -0.13 for the three methods respectively (the probability of obtaining such a value by chance is 11%). Nonetheless, Figure 3 shows that this correlation is less a systematic trend with μ_0^B than an increased scatter in $\mathrm{I_{int}/I_{B_{26}}}$ toward lower surface brightness galaxies, such that the integrated aperture is more likely to be representative of the total B_{26} light for galaxies with the highest central surface brightness.

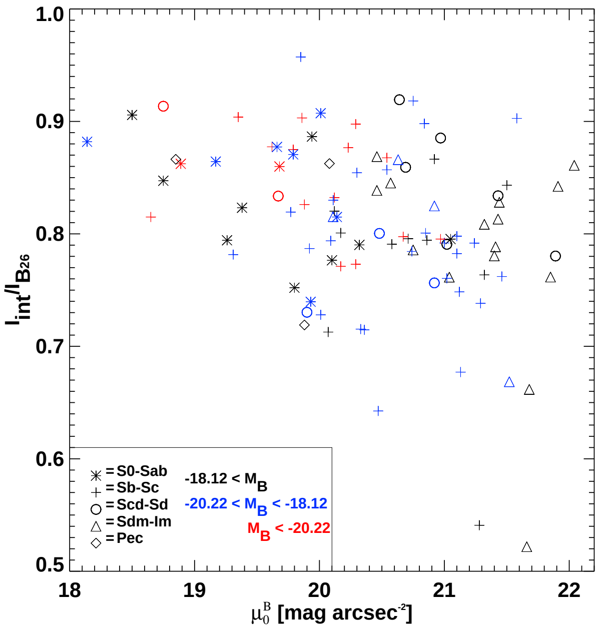

FIG. 3.— The fraction of B_{26} light captured within our integrated spectral aperture compared with the B-band central surface brightness μ_0^B [mag arcsec^{-2}]. We find a mild trend towards lower average integrated B_{26} fractions and a larger range in integrated B_{26} fractions for lower surface brightness galaxies.

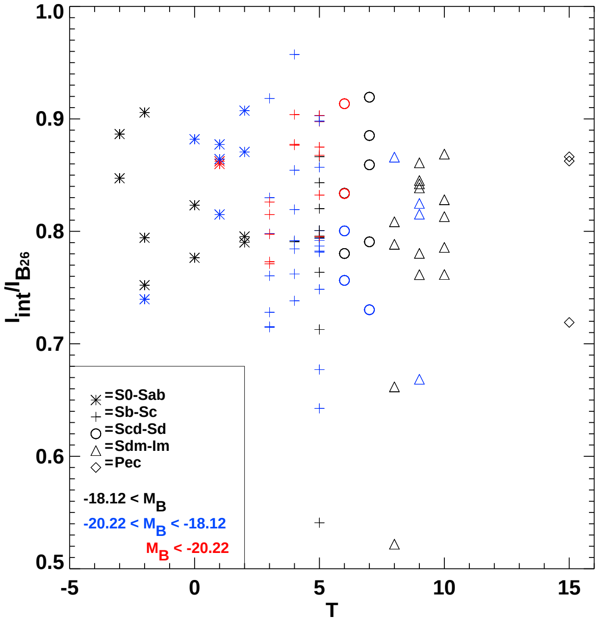

FIG. 4.— The fraction of B_{26} light captured within our integrated spectral aperture compared with numeric morphological type T from (Jansen et al. 2000a). We find no statistically significant dependence of $I_{int}/I_{B_{26}}$ on morphological type.

Figure 4 shows the range in $I_{int}/I_{B_{26}}$ as a function of numeric morphological type, T, described in (Jansen et al. 2000a). There is no statistically significant systematic offset between the $I_{int}/I_{B_{26}}$ values as a function of numeric type.

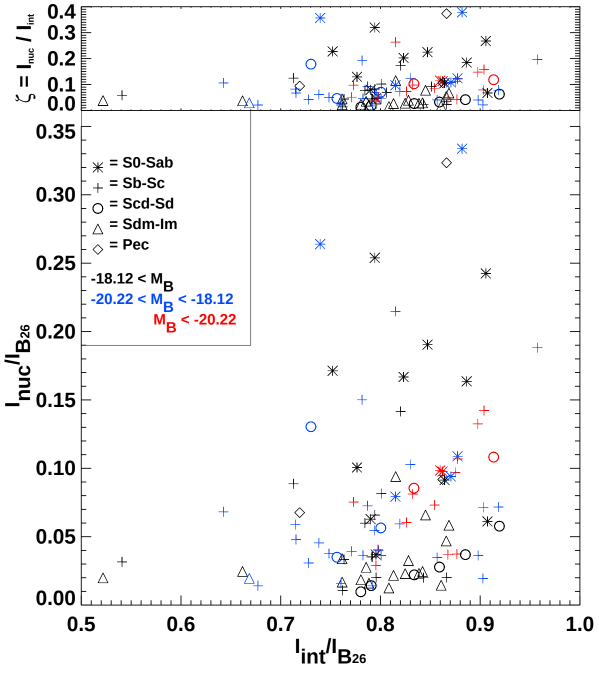

FIG. 5.— Bottom Panel: Comparison between the nuclear and integrated B_{26} flux covering fractions for the 101 NFGS galaxies in our sample. Symbol shapes and colors are encoded according to Hubble type and luminosity range shown in the legend. The average integrated flux covering fraction is ∼ 0.81 nuclear slit flux covering fraction is ∼ 0.07. The rms scatter for both is 0.07. Top Panel: The relative nuclear/integrated B_{26} covering fraction (ζ) versus the integrated B_{26} covering fraction. The relative B_{26} covering fraction ranges between 0-0.4.

3.2. *Nuclear versus Integrated Flux Coverage*

Figure 5 compares the range in the fraction of B_{26} light captured by the nuclear aperture, $I_{nuc}/I_{B_{26}}$, to the fraction of B_{26} light contained within the integrated aperture, $I_{int}/I_{B_{26}}$, for our 101-galaxy sample. The nuclear spectra capture a significantly larger fraction of the B_{26} light for early- (S0–Sab) than for late-type (Sb–Scd) spiral galaxies. The nuclear B_{26} fraction, $I_{nuc}/I_{B_{26}}$, ranges between 0.01 and 0.33, with an average value of ∼0.07 and an rms scatter of 0.07. The integrated spectra sample a much larger fraction of the B_{26} light: $I_{int}/I_{B_{26}}$ spans the range 0.52–0.96 with an average of 0.81 and an rms scatter of 0.07. For our sample, the average size[2] of the elliptical isophote that encompasses 81% of the B_{26} emission is $21\farcs94\pm0\farcs40$ (with an rms of $9\farcs60$), or ∼4.35 kpc[3].

For the purpose of our analysis, we define the relative nuclear/integrated B_{26} fraction as:

$$\zeta = \frac{(I_{nuc}/I_{B_{26}})}{(I_{int}/I_{B_{26}})} = \frac{I_{nuc}}{I_{int}} \tag{1}$$

---

[2] Throughout, we will express the size of an ellipse with semi-major and -minor axes a and b in terms of the *elliptical* or *equivalent* radius, defined as $r = \sqrt{ab}$.

[3] Note that the physical galaxy sizes have been averaged rather than a mean angular size combined with a mean redshift.

The integrated spectra sample 81.0% of the B_{26} emission on average. Hence the relative nuclear/integrated B_{26} fractions $\zeta = 0.1$, 0.2, 0.3 or 1.0 correspond to 10%, 20%, 30% or 100% of ∼81% of the light encompassed within the B_{26} isophote on average, or equivalently, ∼8.1%, 16.2%, 24.3%, or 81.0% of the total light within the B_{26} isophote. The mean galaxy diameters for our sample that correspond to these ζ are ∼1.4, 2.1, 2.8 and 8.7 kpc.
Table 3 gives the mean ζ and the mean diameter of the B_{26} isophote for early-type spiral galaxies, late-type spirals, and late-type/irregular galaxies (Sdm–Im/Pec). The mean value of ζ for early-type spirals is 0.17, compared with 0.07 for the later types. In our sample, early-type galaxies are on average smaller in angular extent than late-types and their surface brightness profiles are steeper (see Jansen et al. 2000a). Later-type galaxies have shallower profiles, consistent with smaller contributions from a bulge component relative to their disk (e.g., Möllenhoff 2004). In Table 4 we list the mean elliptical radii (in arcseconds) that enclose varying fractions of the B_{26} light, expressed both directly and in terms of the relative nuclear/intergrated B_{26} fraction, ζ. We compute the radii from the radial surface brightness profiles of Jansen et al. (2000a). Because the radii are not directly calculated from the B-band images, they do not take any high spatial frequency substructure into account.

Figure 6 shows the relationship between angular size and redshift for $\zeta = 0.1, 0.2, 0.3$, and 1.0. The solid line represents the mean B_{26} diameter of the NFGS galaxies in our sample (~ 16.2 kpc). Dotted, dashed, dot-dashed,and long-dashed lines correspond to $\zeta = 0.1, 0.2, 0.3$, and 1.0 respectively. The colored symbols on Figure 6 show our 101-galaxy sample, artificially redshifted by requiring that the median redshift of the sample is at $z = 0.3, 0.4, 0.5, 0.6$. The symbols give the Hubble type distribution. Arrows in Figure 6 mark the angular size of the 2dF and SDSS fibers. Clearly, the ζ which would produce a spectrum that mimics our integrated spectrum ($\sim 81\%$) is attained with SDSS fibers at redshifts $z \gtrsim 0.2$ and with 2dF fibers at redshifts $z \gtrsim 0.3$. Samples containing many early-types require a lower redshift to obtain a high ζ with SDSS or 2dF fibers; samples containing many late-types require a larger redshift.

The symbol colors in Figure 6 correspond to the three luminosity bins shown in previous figures. There is a strong dependence of ζ on luminosity. At higher redshift, magnitude limited samples contain galaxies with higher luminosities on average than local samples because the galaxies at the faint end of the luminosity function are missing. Figure 7 shows $\zeta = 0.1, 0.2, 0.3, 1.0$ for the mean diameter of the $M_B < M_\star$ galaxies in our sample. Clearly for samples containing $M < M_\star$ galaxies similar to those in the NFGS, there is no practical redshift which provides a ζ that mimics our integrated spectrum. Figure 7 illustrates the importance of understanding the relationship between the luminosity range of a sample and the flux coverage of the aperture. In the following Sections, we investigate the flux coverage required to provide representative estimates of metallicity, star formation rate and extinction.

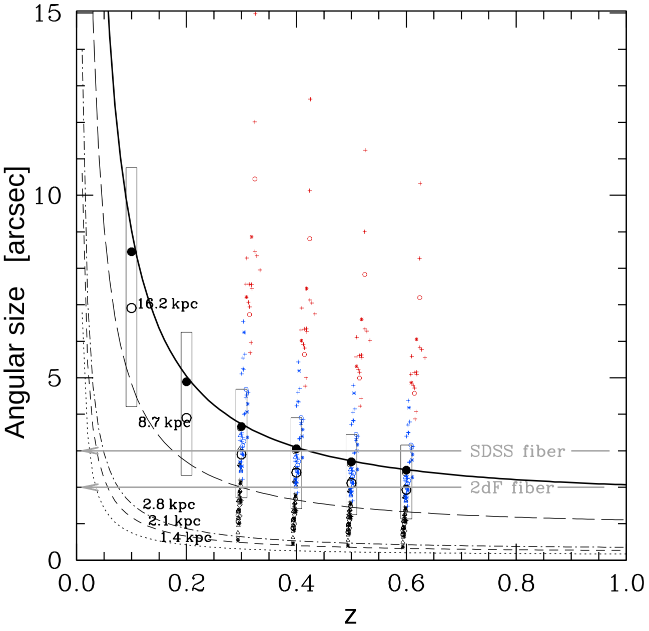

Fig. 6.— Redshift versus angular size (arcseconds) for several values of ζ. We artifically redshifted our 101-galaxy sample by requiring that the median redshift become $z = 0.1$, 0.2, 0.3, 0.4, 0.5 and 0.6. The depth of the sample along the line of sight is preserved. The original selection of the NFGS galaxies is reflected by the slight slant of the data points with respect to the vertical (show only for $z \geq 0.3$), with higher luminosity galaxies (red symbols) being farther away. Luminosity ranges (and corresponding colors) are as in Figure 1. Solid (open) circles represent the mean (median) angular sizes of the B_{26} isophote in the redshifted sample, and the open bars represent the quartile range. The solid curve, represents the mean diameter of the B_{26} isophote (∼16.2 kpc for the un-redshifted sample). Dotted, short-dashed, dot-dashed and long-dashed curves correspond to relative covering fractions $\zeta = 0.1$, 0.2, 0.3 and 1.0, respectively. For a mean NFGS galaxy diameter of ∼16.2 kpc, these values of ζ correspond to 1.4, 2.1, 2.8 and 8.7 kpc, respectively. $\zeta = 1.0$ corresponds to the average fraction of the light that is captured by our integrated spectra, i.e., ∼81% of the total light enclosed by the B_{26} isophote. The angular sizes of the 2dF and SDSS fibers are indicated by the grey arrows for reference. Reliable global metallicities require a minimum ζ of atleast 0.2 (short-dashed line).

In the remainder of this paper, we assume that our integrated spectra are representative of the emission-line properties within the B_{26} isophote. Six galaxies have integrated covering fractions < 0.7, for which this assumption may not be valid. We mark these galaxies in each figure with a circle.

4. METALLICITY

Aperture effects on metallicity estimates result from metallicity gradients. Aller (1942) first noticed gradients in the emission-line ratio [O III]/Hβ within the late-type spiral M33. Searle (1971) then interpreted the radial change in the [O III]/Hβ ratio as a radial decrease in metallicity (O/H). Abundance gradients have now been observed in many galaxies (see Henry & Worthey 1999, for a review). Various hypotheses have been proposed to explain abundance gradients: (1) radial variation of stellar yields caused by IMF differences between the spiral arms and the interarm regions (e.g. Guesten & Mezger 1982); (2) a star formation rate dependence on radius (Phillipps & Edmunds 1991); (3) radial infall of primordial gas during disk formation (Matteucci & François 1989; Pagel 1989;

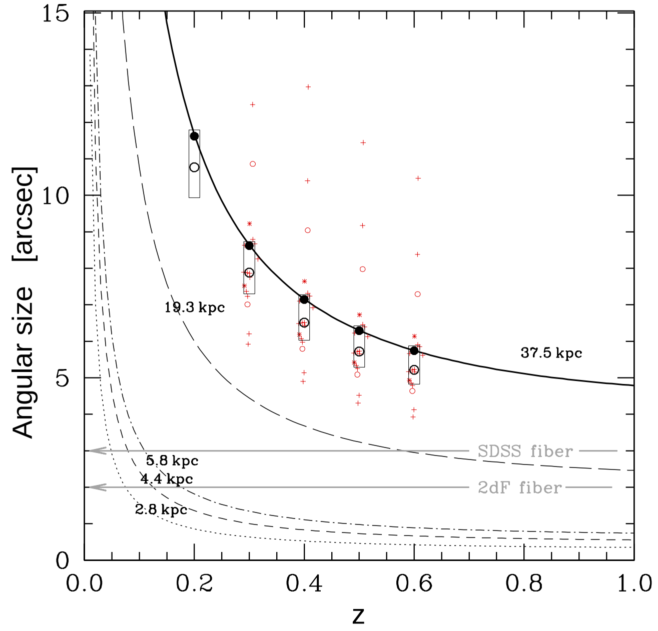

FIG. 7.— Redshift versus angular size (arcseconds) for the high luminosity ($M_B < -20.22$) galaxies in our sample shown in Figure 6 The solid line represents the mean diameter ($\sim$ 16.2 kpc) of the B_{26} isophote for these high luminosity galaxies. Dotted, short-dashed, and dot-dashed, and long dashed lines correspond to B_{26} relative covering fractions $\zeta = 0.1, 0.2, 0.3$ and 1.0, respectively. These values of ζ correspond to diameters of 2.8, 4.4, 5.8, and 19.3 kpc. $\zeta = 1.0$ corresponds to the average fraction of the light that is captured by our integrated spectra, i.e., ~81% of the total light enclosed by the B_{26} isophote. The angular size of the 2dF and SDSS fibers are marked (grey arrows). Reliable global metallicities require a minimum ζ of atleast 0.2 (short-dashed line).

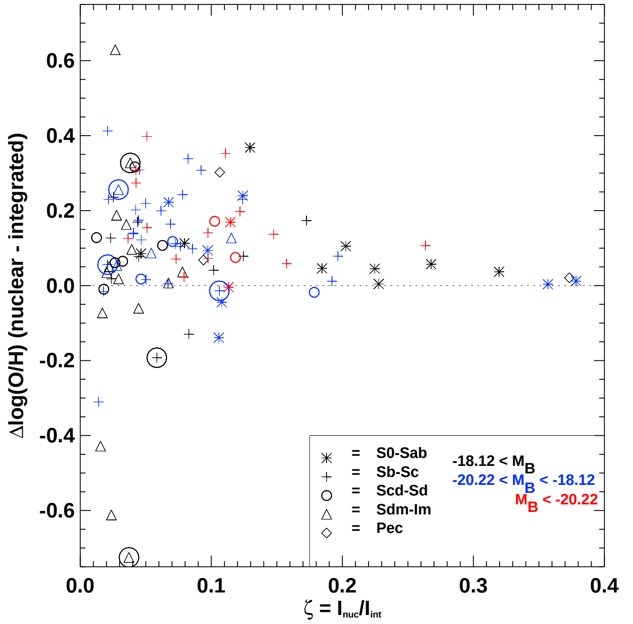

FIG. 8.— Abundance ratio (nuclear/integrated) in log units versus the relative (nuclear/integrated) B_{26} covering fraction ζ for the NFGS galaxies as a function of Hubble type and luminosity at a fixed ζ. The six galaxies with integrated B_{26} fractions $I_{int}/I_{B_{26}} < 0.7$ are marked with a large circle. For small ζ (0-0.1) the abundance ratio has considerable scatter. The scatter is a function of galaxy type. With small apertures ($\lesssim$ 10% of the light) the metallicity is systematically over-estimated for most galaxies. Although errors in the absolute metallicities are ~ 0.1 in log(O/H)+12 units, these errors primarily reflect the accuracy of the theoretical models used to create the metallicity diagnostics. Any error introduced by the diagnostics is likely to be systematic (see Kewley et al. 2002; Kobulnicky & Kewley 2004, for a discussion). Because we are using *the same* metallicity diagnostic for both nuclear and integrated spectra, errors in the *relative* metallicities should be $\ll 0.1$ dex.

Edmunds & Greenhow 1995). Current chemical evolution models include a combination of these three processes (e.g., Churches, Nelson, & Edmunds 2001).

The dependence of the metallicity gradient on galaxy type is unknown. Massive late-type spirals like M101 have large metallicity gradients; the H II region metallicities decrease by an order of magnitude from the inner to the outer disk (see e.g., Shields 1990, for a review). However, not all galaxies have strong metallicity gradients. Many barred spiral galaxies have weaker metallicity gradients than spirals of similar type (e.g., Pagel et al. 1979; Roy& Walsh 1997), suggesting that radial gas flows suppress or mix metallicity gradients (Roberts, Huntley, & van Albada 1979; Martin & Roy 1994; Roy& Walsh 1997, e.g.,) (but c.f. Considère et al. 2000)

Despite numerous studies, it is unclear whether early-type spiral galaxies have weaker metallicity gradients than late types. Metallicity gradient comparisons may be affected by variations in mass, luminosity and gas fraction, as well as dynamical effects such as radial gas flows (see e.g., Mollá, Ferrini, & Díaz 1996, for a review). Smith (1975) found weaker gradients in early-type spirals than in late types. However, Edmunds (1984) argued that the metallicity gradient in early-types is similar to that in late types. Garnett & Shields (1987) showed that the Sab galaxy M81 has a similar gradient to the gradients observed in later-type spirals with similar mass, luminosity, and gas fraction.

These complex metallicity gradients may introduce random and/or systematic errors into the luminosity-metallicity relation found in fiber surveys (Tremonti et al. 2004; Lamareille et al. 2004; Maier, Meisenheimer, & Hippelein 2004). The combination of strong metallicity gradients with a small fixed-angular size aperture may produce a decrease in global galaxy metallicities with increasing redshift until the aperture size is comparable to the galaxy size. On the other hand, weak metallicity gradients may have little or no effect on metallicities obtained with a small fixed-angular size aperture.

Figure 8 shows the metallicity ratio (nuclear metallicity - integrated metallicity in log(O/H) units) versus ζ for the Hubble types and luminosity ranges in our sample. Use of ζ as a covering fraction diagnostic assumes that our integrated spectra are representative of the total emission within the B_{26} isophotal radius. The dotted line shows where the data would lie if the nuclear and integrated metallicities were identical. The nuclear metallicities exceed the integrated metallicities on average by ~ 0.13 dex for our 101-galaxy sample.

The inclination of the galaxies (whether a galaxy is viewed face-on or edge-on) may influence whether a

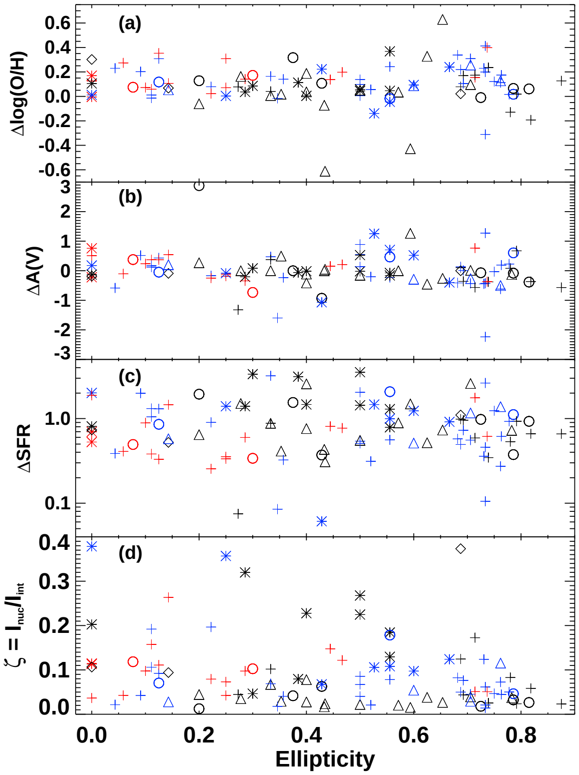

FIG. 9.— Ellipticity from Jansen et al. (2000a) versus (a) Abundance ratio (nuclear/integrated) in log units, (b) Nuclear - integrated extinction A(V), (c) SFR ratio (nuclear/integrated), and (d) relative (nuclear/integrated) B_{26} covering fraction ζ. There is no clear correlation between ellipticity and abundance ratio, extinction ratio, SFR ratio, or covering fraction.

strong abundance gradient is observed. In Figure 9a we plot ellipticity versus metallicity ratio. There is no correlation between ellipticity and nuclear to integrated metallicity ratio. Because ellipticity is only a very crude measure of inclination, a lack of correlation between ellipticity and metallicity ratio does not rule out a correlation between inclination and metallicity ratio.

For small ζ (0-0.1), the metallicity ratio has a large scatter. Table 3 gives the mean and rms scatter in ζ and metallicity ratio for early type spirals (S0-Sab), late type spirals (Sb-Sd) and very late Hubble types (Sdm-Im/Pec). Clearly the galaxy distribution in Figure 8 is influenced by Hubble type and luminosity. The mean metallicity ratio for late types (Sb-Sd) is 0.14 ± 0.02 dex compared with 0.09 ± 0.03 dex for the early types (S0-Sab) and 0.11 ± 0.06 dex for the very late types (Sdm-Im-Pec). We note that the NFGS early-type galaxies have larger ζ on average than the later galaxy types. The minimum ζ for early-types is 0.046. For $0.046 < \zeta < 0.15$, the difference between the early, late-type and very late-type mean metallicity ratios is not significant within the errors (0.13 ± 0.05, 0.14 ± 0.02, 0.11 ± 0.05).

Figure 8 and Table 3 show that the very late-type galaxies show considerably more scatter in metallicity ratio than early types or late-types. This difference is dominated by the 4 Sdm-Im galaxies with small ζ; for $0.046 < \zeta < 0.15$, the early-types and late types have comparable scatter about their mean metallicity to the very late-types (0.13-0.14 c.f. 0.10). However, a larger sample of early-types is required to judge whether the difference in scatter at small ζ is significant. Table 5 gives the fraction of galaxies of each Hubble type within three luminosity ranges. The Sdm, Im, and Peculiar galaxies have the smallest range in luminosities, with the majority of luminosities $M_B > -18.12$. Low-luminosity Sdm, Im, and Peculiar galaxies often have diffuse or patchy star-formation distributions that may result in a wide range of metallicity gradient slopes (see Figure 2.3 in Jansen et al. 2000a). A patchy metallicity distribution might result from randomly distributed star forming regions with a relatively long time between bursts.

4.1. *Effect of Aperture on Metallicity*

Figure 8 and Table 3 show that if $\zeta \lesssim 0.2$, the estimated metallicity exceeds the global metallicity by ~ 0.13 dex (log(O/H) units) on average. The range in metallicity gradients observed in galaxies (i.e., the scatter in Figure 8) introduces an error up to ± 0.6 dex in metallicity. As ζ increases from 0.01 to 0.4, the scatter decreases and the metallicity ratio tends towards zero. The data suggest that a flux covering fraction of $\zeta > 0.2$ (i.e. $\gtrsim 20\%$ of the galaxy B_{26} light) is required for a reliable indication of the global metallicity value. We note that only a small fraction of our sample (9 galaxies) have $\zeta > 0.2$. The majority (6/8) of these galaxies are early-type spirals. A similar number of early-type spirals in our sample have $\zeta < 0.2$ (11 galaxies). If the reduction in scatter for $\zeta > 0.2$ is not real, then we would expect the scatter to be similar for the early-types with $\zeta < 0.2$ and the early-types with $\zeta > 0.2$. The rms scatter for early-types for $\zeta < 0.2$ is 0.14 compared to 0.03 for $\zeta > 0.2$, indicating that the reduction in scatter for $\zeta > 0.2$ is likely to be real. For other galaxy types, our results indicate that an aperture which contains less than 20% of the global galaxy B_{26} light is inadequate. A larger sample is required to verify the specific aperture size at which the metallicities will approximate the global values.

For the SDSS fiber, a redshift $z \gtrsim 0.04$ is required to reach $\zeta \gtrsim 0.2$, assuming the SDSS samples cover a similar range of luminosity and Hubble type as our sample. For the 2dF fiber, a redshift $z \gtrsim 0.06$ is required. If metallicities are estimated using strong-line ratios from the SDSS or 2dF fiber spectra for objects at redshifts $z \lesssim 0.04$ or $z \lesssim 0.06$ respectively, errors in the metallicity estimates could be significant (up to ± 0.6 dex in log(O/H)), and metallicities are likely to be systematically over-estimated by $\sim$ 0.13 dex on average if the late-type fraction is similar to the NFGS. The situation is worse for high luminosity samples. For SDSS samples with a mean luminosity $L > L_\star$, a redshift of $z \gtrsim 0.09$ is required to reach $\zeta \gtrsim 0.2$. For 2dFGRS samples, with $L > L_\star$, a a redshift of $z \gtrsim 0.14$ is required. Note that more conservative (i.e. larger) lower limits on z are required to ensure that most galaxies (not just the typical galaxy) in a given sample yield reliable metallicity estimates.

4.2. *Implications for the Luminosity-Metallicity Relation*

Recent investigations into the luminosity-metallicity relation using fiber surveys may be affected by the metallicity gradient aperture effect. For galaxies at the same z, the aperture effect is larger at higher luminosities. This problem may affect the slope of luminosity-metallicity relations.

Lamareille et al. (2004) calculated the luminosity-metallicity relation for 6387 2dFGRS galaxies between redshifts of $0 < z < 0.15$, with a median redshift of 0.11. The redshift limit of $z = 0.15$ corresponds to our B_{26} covering fraction of $\sim 50\%$ and $\zeta \sim 0.6$, assuming that the median size, luminosity and type of the 2dFGRS galaxies is the same as in the NFGS sample. The median redshift of the 2dFGRS sample corresponds to a $\zeta \sim 0.45$. It is likely therefore that a minor fraction of the 2dFGRS metallicities (galaxies at redshifts $\lesssim 0.06$) are affected by the aperture-metallicity effect (Figure 8). The galaxies at redshifts < 0.06 may have apparent metallicities higher than their global metallicities by ~ 0.1 dex on average with a large scatter introduced by aperture effects and metallicity gradients.

Schulte-Ladbeck et al. (2004) calculated the SDSS luminosity-metallicity relation for 13,000 SDSS galaxies between redshifts of $0 < z < 0.3$. They show luminosity-metallicity plots for large, small and compact star-forming galaxies within four redshift ranges: $0 < z \leq 0.05$, $0.05 < z \leq 0.1$, $0.1 < z \leq 0.2$ and $0.2 < z \leq 0.3$. The $3''$ SDSS fiber produces a $\zeta \lesssim 0.15$ for the redshift range $0 < z \leq 0.05$ for the typical diameter of our NFGS sample. In this redshift range, the SDSS late-type star-forming galaxies may have metallicities that are overestimated compared to their global metallicities. In addition, the metallicity estimates of the late-types and very-late types in the SDSS sample are probably prone to the large scatter that we observe in Figure 8 at small ζ. The $0 < z \leq 0.05$ luminosity-metallicity relation is probably dominated by aperture effects. Figure 6 indicates that the remaining redshift ranges in Schulte-Ladbeck et al. are probably not strongly influenced by aperture effects except possibly at the highest luminosities, unless their galaxy properties differ significantly from those in the NFGS, and/or our chosen minimum covering fraction of $\zeta > 0.2$ is too low for late type galaxies that are not well represented in our $\zeta > 0.2$ sample.

Tremonti et al. (2004) used 210,000 SDSS galaxies with redshifts between $0.03 < z < 0.25$ to calculate the luminosity-metallicity and mass-metallicity relations. They selected this redshift range to minimize aperture effects. As a result of this selection criterion, the SDSS luminosity-metallicity and mass-metallicity relations are probably not seriously affected by a metallicity gradient aperture effect.

We note that luminosity-metallicity relations are very sensitive to the choice of metallicity diagnostic; different diagnostics can produce metallicity estimates that differ systematically by $\sim 0.1 - 0.2$ dex (e.g., Kewley & Dopita 2002). Therefore, differences between Lamareille et al. (2004) and other luminosity-metallicity relations may be influenced by the choice of metallicity diagnostic as well as by the aperture-metallicity effect.

We conclude that comparison of luminosity-metallicity relations requires (1) careful attention to aperture effects, particularly to the dependence of these effects on luminosity, and (2) use of the same metallicity diagnostic.

5. EXTINCTION

Dust grains form from heavy elements. Thus one might expect an extinction gradient in disk galaxies similar to the metallicity gradient (unless the dust grains are depleted from the H II regions). Observations of extinction in H II regions of disk galaxies give conflicting results. Sarazin (1976) used radio and optical observations to show that extinction gradients exist in M101 and M33. These gradients were confirmed by Viallefond & Goss (1986) and Israel & Kennicutt (1980). More recently, Jansen et al. (1994) and Roy& Walsh (1997) reached similar conclusions. Jansen et al. (1994) showed that similar extinction gradients exist in three highly-inclined spiral galaxies to those in our Galaxy and in the Sombrero galaxy. Roy& Walsh (1997) examined the extinction gradient in the barred spiral galaxy NGC 1365 and showed that the extinction decreases 0.4-0.6 mag from the nucleus to the edge of the disk. However, Kaufman et al. (1987) found a significant scatter in radio-derived extinction measurements for H II regions in the disk of the early-type spiral galaxy M81. Kaufman et al. ascribed this scatter to a patchy dust distribution external to the H II regions. They found little evidence for a strong extinction gradient, in contrast with the previous work on M33 and M101. We note that M81 is a member of an interacting triplet and its extinction properties may be influenced by the interaction. However, Kennicutt, Keel & Blaha (1989) reached conclusions similar to Kaufman et al. in their comparison between various H II region-like nuclei and disk H II regions. Kennicutt et al. tentatively conclude that although optical extinction (derived from the Balmer decrement) is important for individual H II regions and nuclei, the effect of extinction between nuclear and disk H II regions is similar.

Figure 10 shows the nuclear - integrated $A(V)$ versus ζ. Table 3 gives the mean $\Delta A(V)$ and the scatter about the mean for the early, late, and very late type galaxies. As we have discussed in Section 2, a number of galaxies in our sample have intrinsically low reddening, with an upper limit of $E(B-V) < 0.02$ ($A(V) = 0.061$) for their integrated and/or nuclear spectra. We calculated the mean and rms $\Delta A(V)$ for $A(V) = 0.061$ and $A(V) = 0.0$. The difference between using $A(V) = 0.061$ or $A(V) = 0.0$ is smaller than the size of the data points in Figure 10 and the effect on $A(V)$ properties in Table 3 is negligible.

In Figure 9b we plot ellipticity versus $\Delta A(V)$. There is no correlation between ellipticity and $\Delta A(V)$ but this result does not rule out a correlation between inclination and $\Delta A(V)$.

The sample mean $\Delta A(V)$ is consistent with ~ 0 within the errors, indicating that there is no significant offset between the nuclear and integrated $A(V)$ on average. This result is consistent with the flat extinction gradients observed by Kennicutt, Keel & Blaha (1989) and Kaufman et al. (1987), but our result appears to be inconsistent with the extinction gradients observed with radio data for M101 and M33. However, radio-derived extinction measurements are known to systematically exceed those calculated using the Balmer decrement for the

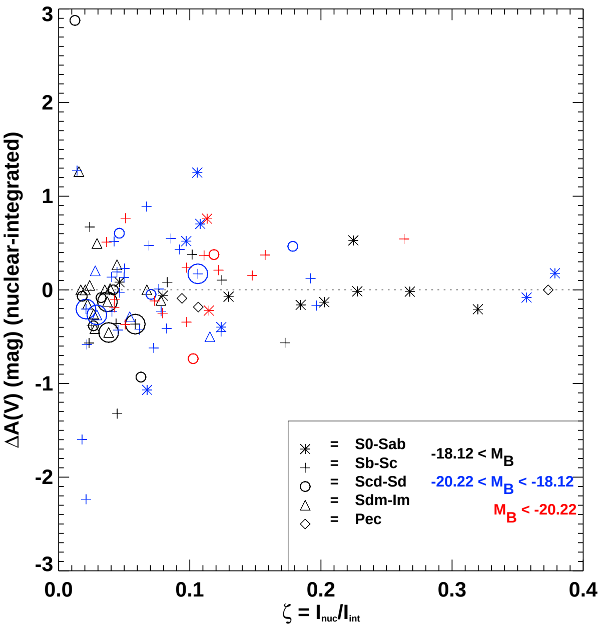

FIG. 10.— Nuclear - integrated extinction A(V) versus the relative (nuclear/integrated) B_{26} covering fraction ζ for the NFGS galaxies as a function of Hubble type. The six galaxies with integrated B_{26} fractions $I_{int}/I_{B_{26}} < 0.7$ are marked with a large circle. For small ζ (0.01-0.1) ΔA(V) has considerable scatter. The estimated error in ΔA(V) is ±0.09.

same H II regions (e.g., Sarazin 1976; Israel & Kennicutt 1980; Caplan & Deharveng 1986; van der Hulst et al. 1988; Kennicutt, Keel & Blaha 1989; Bell et al. 2002). Indeed, radio continuum fluxes predict a higher extinction in H II nuclei than in disk H II regions, even though the extinction measured using the Balmer decrement is similar (with large scatter) for nuclear and disk H II regions (Kennicutt, Keel & Blaha 1989). Kennicutt et al. attributed this discrepancy to low-level AGN contribution. However a similar discrepancy is seen in the Magellanic Clouds HII regions study by Bell et al. (2002). The cause of this discrepancy is unknown. A lower Balmer decrement extinction estimate may result from the presence of dust grains with a flat optical absorption curve (Sarazin 1976), or an inhomogeneous (clumpy) distribution of absorbing material/dust (Sarazin 1976; Caplan & Deharveng 1986; Kaufman et al. 1987; van der Hulst et al. 1988). The presence of clumpy dust may cause scatter in Figure 10. Systematic effects on the optical Balmer decrement are likely to be minimized in Figure 10 because we use the ratio of the nuclear to integrated Balmer decrement where both the nuclear and integrated Balmer decrements are derived using the same method.

5.1. *Effect of Aperture on Extinction*

Figure 10 indicates that for $\zeta < 0.2$, the extinction for an individual galaxy may be overestimated or underestimated by up to 1 mag. If ζ is very small ($\lesssim 0.03$), the extinction may be up to 3 magnitudes smaller or larger than the global value. Late-type galaxies are probably more strongly affected by this aperture effect than early or very late types; late type galaxies have the largest scatter in $\Delta A(V)$ (0.7 rms vs. 0.4-0.5 rms). The best global extinction estimates from the 2dFGRS and SDSS are likely to occur at redshifts $\gtrsim 0.06$ and redshifts $\gtrsim 0.04$, respectively (Figure 6) for samples with similar properties to the NFGS. Samples containing higher luminosity galaxies, or many late-type galaxies require larger minimum redshift limits.

6. STAR FORMATION RATE

Metallicity and extinction estimates are usually calculated using emission-line ratios that have not been corrected for metallicity or extinction gradients because these gradients are not known a priori. Optical star formation-rates, on the other hand, require emission-line luminosities. The effect of aperture on emission-line luminosities can lead to strong biases in star-formation rate studies. The potential implications of these biases are discussed by several authors (Gómez et al. 2003; Pérez-González et al. 2003; Hopkins et al. 2003; Nakamura et al. 2003).

To avoid strong biases, the luminosities and star-formation rates derived from fiber surveys are corrected for aperture effects. The simplest aperture correction methods assume that the emission measured through the fiber is representative of the entire galaxy. One such method was applied to the SDSS Hα and [O II] SFRs by Hopkins et al. (2003) (hereafter H03). H03 multiplied the emission-line equivalent widths by the flux at the effective wavelength of the SDSS r-band filter. H03 also applied a more explicit aperture correction A based on the difference between the total galaxy magnitude $\mathrm{r}_{\mathrm{total}}$ and the magnitude calculated from the fiber spectrum $\mathrm{r}_{\mathrm{fiber}}$:

$$A = 10^{-0.4(\mathrm{r}_{\mathrm{total}} - \mathrm{r}_{\mathrm{fiber}})}. \quad (2)$$

This technique is roughly equivalent to multiplying our NFGS nuclear fluxes by the ratio of the integrated to nuclear covering fractions. Both of the methods outlined in H03 assume that the distribution of the line emission (active star formation regions) is identical to that of the stellar continuum emission (older stellar population). However. Hα and r-band continuum images of spiral galaxies show marked differences. Lehnert & Heckman (1996) showed that spiral galaxies selected to have regular symmetric profiles in r-band continuum images do not have regular, symmetric Hα+[N II] emission. Rather, the Hα+[N II] emission appears clumpy with filaments. In some cases, the Hα+[N II] emission forms large-scale regions with bubble and/or shell-like structures. Even early-type spirals show very diverse Hα morphologies, despite similar $r-$band continuum morphologies (Hameed & Devereux 1999).

Brinchmann et al. (2004) proposed a more complex aperture correction method. They calculate the likelihood distribution of the star formation rate for a given set of spectra with global and fiber $g-r$ and $r-i$ colours. Brinchmann et al. tested this method using galaxies within the SDSS with different fiber covering fractions. They conclude that their correction method is robust only if $\geq$ 20% of the total r-band light is sampled by the fiber, in remarkable agreement with our conclusions for metallicity and extinction.

We calculate star-formation rates for our NFGS sample using the Hα luminosities and the Kennicutt (1998)

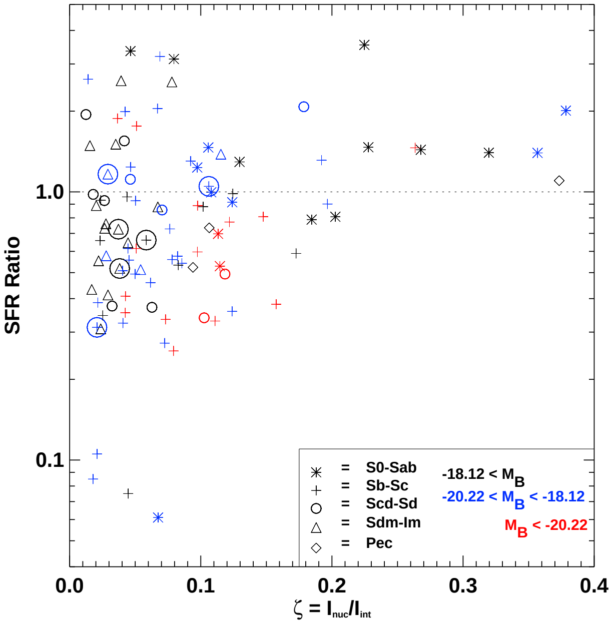

Fig. 11.— SFR ratio (nuclear/integrated) versus the relative (nuclear/integrated) B_{26} covering fraction ζ for the NFGS galaxies as a function of Hubble type. The six galaxies with integrated B_{26} fractions $\mathrm{I_{int}/I_{B_{26}}} < 0.7$ are marked with a large circle. For small ζ (0.01-0.2) the SFR ratio has considerable scatter. The scatter is a function of galaxy type. The estimated error in the SFR from Hα for the NFGS is $\sim 30\%$.

SFR(Hα) calibration (as described in Kewley et al. 2002). To simulate the effect of the simple aperture correction methods of H03, we multiply our nuclear SFRs by the ratio of the corresponding integrated to nuclear covering fractions. This process provides crude ‘expected’ global SFR estimates for comparison with SFRs derived from our integrated spectra.

In Figure 9c we plot ellipticity versus the ratio of ‘expected’ to integrated Hα star formation rates (SFR ratio). There is no correlation between ellipticity and SFR ratio but this result does not rule out a correlation between inclination and SFR ratio.

Figure 11 shows the ratio of expected to integrated Hα star formation rates versus ζ. Table 3 gives the mean and rms scatter for the early, late and very late types. The mean SFR ratio for early-type spirals is 1.47 ± 0.23. A mean SFR ratio > 1 indicates that SFRs calculated by this widely used prescription overestimate the true global SFRs on average, despite the fact that the early types have a larger ζ (0.17 c.f. 0.07). H03 found a similar effect when they compared their Hα SFRs with those measured using the radio 1.4GHz flux. The H03 Hα SFRs are overestimated for galaxies requiring the largest aperture corrections. The largest galaxies typically require the largest aperture corrections. The expected SFRs may be overestimated if the star-forming regions in early-types are centrally concentrated (Hameed & Devereux 1999; James et al. 2004).

The mean SFR ratio for the late-types is 0.85 ± 0.08, implying that we miss $\sim 10{-}20\%$ of the star formation by assuming that the emission-line gas follows an identical profile to the continuum emission. Star formation that is extended or that occurs preferentially in the outer regions of late type galaxies probably explains this result (e.g., Bendo et al. 2002).

For small $\zeta < 0.2$, there is substantial scatter between the nuclear and integrated SFR measurements (rms scatter = 0.70). We therefore recommend that SFR studies use spectra with $\zeta > 0.2$, confirming the conclusion of Brinchmann et al. (2004).

For $\zeta > 0.2$, although the scatter is reduced, there is a danger that the expected SFR value over-estimates the true SFR. For $\zeta > 0.2$ the corrected small aperture measurement predicts a value that is $60 \pm 20\%$ larger than our integrated spectrum, even when the aperture ζ approaches 0.4. Only 8 galaxies in our sample have $\zeta > 0.2$ and most of these galaxies are early-types. A larger sample of galaxies with flux covering fractions between 0.2-1 is required to determine whether this SFR overestimate is a serious concern. However, these results serve as a warning that there is danger in determining the global SFR by applying a simple aperture correction, even for ζ as large as 0.4. Note that in a fixed aperture fiber survey galaxies with higher luminosities or late-type galaxies need to be at a larger redshift to ensure that $\zeta > 0.2$.

7. IMPLICATIONS FOR STAR FORMATION HISTORY STUDIES

Some fiber-based SFR studies cover redshifts $z > 0.05$ to minimize the potential aperture bias (Gómez et al. 2003; Brinchmann et al. 2004). As we discussed in Section 4.2, a redshift of $z > 0.05$ corresponds to mean $\zeta > 0.2$ for the SDSS. Figure 11 and the results of Brinchmann et al. show that $\zeta > 0.2$ is sufficient to avoid the strong scatter introduced with smaller flux covering fractions. However, SFR calculations that assume identical Hα-emission and continuum distributions may systematically overestimate SDSS SFRs up to redshifts of at least $z = 0.1$ (assuming a 17.7 kpc B_{26} isophotal diameter galaxy), especially if the galaxies contain star-forming regions that are more centrally concentrated than the continuum emission. Care should be taken when comparing star-formation rates derived from emission-lines in fiber surveys and those obtained with larger apertures or by photometric methods.

8. CONCLUSIONS

We investigate the effect of aperture size on the star formation rate, metallicity and extinction for 101 galaxies from the objectively selected Nearby Field Galaxy Survey. Our sample includes galaxies of all Hubble types except ellipticals with SFRs ranging from 0.01 to 100 $\mathrm{M_\odot yr^{-1}}$ and spans a large range in metallicity, star-formation rate and extinction. We calculate an ‘expected’ star formation rate using nuclear spectra and applying the commonly-used aperture correction method. We compare the metallicity, extinction and star formation rate derived from nuclear spectra to those derived from integrated spectra. We find that:

- For flux covering fractions $< 20\%$ ($\zeta < 0.2$) the difference between the nuclear and global metallicity, extinction and star formation rate is substantial. An aperture that contains less than 20% of the B_{26} light is inadequate at providing reliable estimates of the global metallicity, SFR or extinction.

A larger sample of galaxies is required to determine the specific aperture size at which the metallicity, extinction, and star formation rates will approximate the global values.

- For flux covering fractions $< 20\%$, the aperture effect on metallicity depends on Hubble type. This dependence occurs because of differences in the metallicity gradients. Late-type spiral galaxies show the largest systematic difference (~ 0.14 dex) between nuclear and global metallicities. The largest difference (scatter) between the nuclear and global metallicities occurs for Sdm–Im, and Peculiar galaxies, indicating a large range in metallicity gradients for these galaxy types.
- We find little evidence for systematic differences between nuclear and global extinction estimates for any galaxy type. However, there is significant scatter between the nuclear and integrated extinction estimates for flux covering fractions $< 20\%$.
- The 'expected' star formation rate overestimates the global value for early-type spirals and a slightly underestimates the global value for late-type spirals, but with large scatter. The systematic differences probably result from the aperture correction assumption that the distributions of the emission-line gas and the continuum are identical. The large scatter (error) in the estimated SFR occurs when the aperture covering fraction is $< 20\%$.

These aperture effects impact investigations into the luminosity-metallicity relation and star-formation history using fiber surveys unless samples have been selected with a lower limit on z. To avoid the systematic and random errors from aperture effects, we recommend selecting samples with fiber covering fractions that capture $> 20\%$ of the galaxy light. Redshifts $z > 0.04$ and $z > 0.06$ are required to minimize these aperture effects in the Sloan Digital Sky Survey and the 2dF Galaxy Redshift Survey respectively, assuming that these samples contain galaxies with similar properties to those in the NFGS. Samples containing galaxies with higher luminosities and samples containing more late-type galaxies than in the NFGS require larger redshift limits.

We wish to thank the anonymous referee for his/her careful reading of the manuscript and useful comments. L. J. Kewley is supported by a Harvard-Smithsonian CfA Fellowship. M. J. Geller is supported by the Smithsonian Institution.

REFERENCES

Aller, L. H. 1942, ApJ, 95, 52

Baldry, I. K., et al. 2002, ApJ, 569, 582

Bendo, G. J. et al. 2002, AJ, 124, 1380

Brinchmann, J., Charlot, S., White, S. D. M., Tremonti, C., Kauffmann, G., Heckman, T., & Brinkmann, J. 2004, MNRAS, 351, 1151

Burnstein, D. & Heiles, C. 1984, ApJS, 54, 33

Bell, E. F., Gordon, K. D., Kennicutt, R. C., Jr., Zaritsky, D. 2002, ApJ, 565, 994

Caplan, J. & Deharveng, L. 1986, A&A, 155, 297

Cardelli, J. A., Clayton, G. C., & Mathis, J. S. 1989, ApJ, 345, 245

Churches, D. K., Nelson, A. H., & Edmunds, M. G. 2001, MNRAS, 327, 610

Considère, S., Coziol, R., Contini, T., & Davoust, E. 2000, A&A, 356, 89

Davis, M. & Peebles, P. J. M. 1983, ApJ, 267, 465

Dopita, M. A., Kewley, L. J., Heisler, C. A., & Sutherland, R. S. 2000, ApJ, 542,224

Edmunds, B. E. J. 1984, MNRAS, 211, 507

Edmunds, M . G. & Greenhow, R. M. 1995, MNRAS, 272, 241

Garnett, D. R. & Shields, . A. 1987, ApJ, 317, 82

Gómez, P. L. et al. 2003, ApJ, 584, 210

Guesten, R. & Mezger, P. G. 1982, Vistas Astron., 26, 159

Hameed, S. & Devereux, N. 1999, AJ, 118, 730

Henry, R. B. C & Worthey, G. 1999, PASP, 111, 919

Hill, T. L., Heisler, C. A., Sutherland, R. S., & Hunstead, R. W. 1999, AJ, 117, 111

Hodge, P. W. 1963, AJ, 68, 237

Hopkins, A. M., Miller, C. J., Nichol, R. C., Connolly, A. J., Bernardi, M., Gómez, P. L., Goto, T., Tremonti, C. A., Brinkmann, J., Ivezic, Z., & Lamb, D. Q. 2003, ApJ, 599, 971

Huchra, J., Davis, M., Latham, D., & Tonry, J. 1983, ApJS, 52, 89

Israel, F. P. & Kennicutt, R. C. 1980, ApJ, 21, 1

James, P. A. et al. 2004, A&A, 414, 23

Jansen, R. A., Knapen, J. H., Beckman, J. E., Peletier, R. F. & Hes, R. 1994, MNRAS, 270, 373

Jansen, R. A., Franx, M., Fabricant, D., & Caldwell, N. 2000a, ApJS, 126, 271

Jansen, R. A., Fabricant, D., Franx, M., & Caldwell, N. 2000b, ApJS, 126, 331

Jensen, E. B., Strom, K. M., & Strom, S. E. 1976, ApJ, 209, 748

Kaufman, M., Bash, F., Kennicutt, R. C., & Hodge, P. W. 1987, ApJ, 319, 61

Kennicutt, R. C. Jr. 1998, ARA&A, 36, 189

Kennicutt, R. C., Keel, W. C., & Blaha, C. A. 1989, AJ, 97, 1022

Kewley, L. J., Geller, M. J., Jansen, R. A., & Dopita, M. A. 2002 AJ, 124, 3135

Kewley, L. J., & Dopita, M. A., 2002 ApJS, 142, 35

Kewley, L. J., Dopita, M. A., Sutherland, R. S., Heisler, C. A., & Trevena, J. 2001a, ApJ, 556, 121

Kewley, L. J., Heisler, C. A., Dopita, M. A., & Lumsden, S. 2001b, ApJS, 132, 37

Kobulnicky, H. A. & Kewley, L. J. 2004, ApJ, in press, astro-ph/0408128

Lamareille, F., Mouhcine, M., Continu, T., Lewis, I., & Maddox, S. 2004, astro-ph/0401615

Lehnert, M. D. & Heckman, T. M. 1996, ApJ, 462, 651

Maier, C., Meisenheimer, K., & Hippelein, H. 2004, astro-ph/0401619

Martin, P. & Roy, J.-R. 1994, ApJ, 424, 599

Marzke, R. O., Huchra, J. P., & Geller, M. J. 1994, ApJ, 428, 43

Marzke, R. O., da Costa, L. N., Pellegrini, P. S., Willmer, C. N. A., Geller, M. J. 1998, ApJ, 503, 617

Matteucci, F., François, P. 1989, MNRAS, 239, 885

Mollá, M., Ferrini, F., & Díaz, A, I. 1996, ApJ, 466, 668

Möllenhoff, C. 2004, A&A, 415, 63

Nakamura, O., Fukugita, M., Brinkmann, J., & Schneider, D. P. 2003, astro-ph/0312519

Oey, M. S. & Kennicutt, R. C. 1993, ApJ, 411, 137

Osterbrock, D. E. 1989, Astro physics of Gaseous Nebulae and Active Galactic Nuclei (Mill Valley; University Science Books)

Pagel, B. E. J., Edmunds, M. G., Blackwell, D. E., Chun, M. S., & Smith, G. 1979, MNRAS, 189, 95

Pagel, B. E. J. 1989, RMxAA, 18, 161

Pérez-González, P. G., Zamorano, J., Gallego, J., Aragón-Salamanca, A., Gil de Paz, A. 2003, ApJ, 591, 827

Phillipps, S. & Edmunds, M. G. 1991, MNRAS, 251, 84

Roberts, W. W., Huntley, J. M., & van Albada, G. D. 1979, ApJ, 233, 67

Roy, J. R. & Walsh, J. R. 1997, MNRAS, 288, 715

Sarazin, C. L. 1976, ApJ, 208, 323

Schlegel, D. J., Finkbeiner, D. P., & Davis, M. 1998, ApJ, 500, 525

Schulte-Ladbeck, R. E., Miller, C. J., Hopp, U., Hopkins, A., Nichol, R. C., Voges, W., & Taotao, F. 2004, astro-ph/0312069

Searle, L. 1971, ApJ, 168, 327

Shields, G. A. 1990, ARA&A, 28, 525

Smith, H. E. 1975, ApJ, 199, 591

Spergel, D. N., Verde, L., Peiris, H. V., et al. 2003, astro-ph/030209 v3

Storchi-Bergmann, T. 1991, MNRAS, 249, 404

Tinsley, B. M. 1971, Ap&SS, 12, 394

Tremonti, C. A., Heckman, T. M., Kauffmann, G., Brinchmann, J., Charlot, S., White, S. D. M., Seibert, M., Peng, E. W., Schegel, D. J., Uomoto, A., Fukugita, M., & Brinkmann, J. 2004, ApJ, *submitted*

van der Hulst, J. M., Kennicutt, R. C., Crane, P. C., & Rots, A. C. 1988, A&A, 195, 38

de Vaucouleurs, G. 1961, ApJS, 5, 233

de Vaucouleurs, G., de Vaucouleurs, A., Corwin, H. G., Jr., Buta, R. J., Paturel, G., & Fouqué, P. 1991, Third Reference Catalogue of Bright Galaxies (New York: Springer)

Viallefond, F. & Goss, W. M. 1986, A&A, 154, 357

Vílchez, J. M., Pagel, B. E. J., Diaz, A. I., Terlevich, E., & Edmunds, M. G. 1988, MNRAS, 235, 633

Zaritsky, D., Zabludoff, A. I., & Willick, J. A. 1995, AJ, 110, 1602

TABLE 1
Classification and Quality Flags for the NFGS

ID	Name	Integrated		Nuclear		Adopted
		Class[a]	Quality[b]	Class[a]	Q[b]	Class[a]
1	A00113+3037	· · ·	· · ·	· · ·	· · ·	...
2	A00289+0556	HII	1	HII	1	HII
3	NGC 193	· · ·	· · ·	· · ·	· · ·	...
4	A00389-0159	HII	1	HII	3	HII
5	A00442+3224	HII	1	HII	3	HII
6	A00510+1225	Sy1	1	Sy1	1	AGN
7	NGC 315	· · ·	· · ·	AGN	· · ·	AGN
8	A00570+1504	AGN	1	AGN	1	AGN
9	A01047+1625	HII	1	· · ·	· · ·	HII
10	NGC 382	· · ·	· · ·	HII	3	HII
11	IC 1639	· · ·	· · ·	· · ·	· · ·	...
12	A01123-0046	Sy1	1	· · ·	· · ·	AGN
13	A01187-0048	· · ·	· · ·	· · ·	· · ·	...
14	NGC 516	· · ·	· · ·	· · ·	· · ·	...
15	A01300+1804	HII	1	HII	1	HII
16	A01344+2838	HII	1	HII	1	HII
17	A01346+0438	HII	1	HII	1	HII
18	A01374+1539B	· · ·	· · ·	· · ·	· · ·	...
19	NGC 695	HII	1	HII	1	HII
20	NGC 784	· · ·	· · ·	· · ·	· · ·	...
21	A02008+2350	HII	1	· · ·	· · ·	HII
22	IC 195	· · ·	· · ·	· · ·	· · ·	...
23	IC 197	HII	1	· · ·	· · ·	HII
24	IC 1776	HII	1	HII	1	HII
25	A02056+1444	HII	1	HII	1	HII
26	NGC 825	· · ·	· · ·	· · ·	· · ·	...
27	NGC 927	HII	3	· · ·	· · ·	· · ·
28	A02257-0134	HII	1	HII	1	HII
29	NGC 984	· · ·	· · ·	AGN	1	AGN
30	NGC 1029	· · ·	· · ·	· · ·	· · ·	...
31	A02464+1807	· · ·	· · ·	· · ·	· · ·	...
32	A02493-0122	HII	1	· · ·	· · ·	HII
33	NGC 1298	· · ·	· · ·	· · ·	· · ·	...
34	A03202-0205	HII	1	HII	1	HII
35	NGC 1552	· · ·	· · ·	AGN	· · ·	AGN
36	NGC 2692	· · ·	· · ·	· · ·	· · ·	...
37	A08567+5242	HII	3	AGN	· · ·	AGN
38	A09045+3328	HII	1	HII	1	HII
39	NGC 2780	HII	3	HII	3	HII
40	A09125+5303	· · ·	· · ·	· · ·	· · ·	...
41	NGC 2799	HII	1	HII	1	HII
42	NGC 2824	· · ·	· · ·	AGN	1	AGN
43	NGC 2844	HII	1	HII	1	HII
44	NGC 3011	AMB	1	AMB	1	AMB
45	NGC 3009	HII	1	HII	3	HII
46	IC 2520	HII	1	HII	1	HII
47	A09557+4758	HII	1	HII	1	HII
48	NGC 3075	HII	1	HII	1	HII
49	A09579+0439	HII	1	HII	3	HII
50	NGC 3104	HII	1	· · ·	· · ·	HII
51	A10042+4716	HII	1	HII	1	HII
52	NGC 3165	HII	1	AMB	1	AMB
53	A10114+0716	HII	1	· · ·	· · ·	HII
54	NGC 3179	· · ·	· · ·	· · ·	· · ·	...
55	A10171+3853	HII	1	HII	1	HII
56	NGC 3213	HII	3	HII	3	HII
57	NGC 3264	HII	1	HII	1	HII
58	NGC 3279	HII	3	HII	1	HII
59	A10321+4649	HII	1	HII	1	HII
60	A10337+1358	HII	1	HII	1	HII
61	IC 2591	HII	1	HII	1	HII
62	A10365+4812	HII	1	HII	1	HII
63	A10368+4811	HII	1	HII	1	HII
64	NGC 3326	HII	3	HII	1	HII
65	A10389+3859	· · ·	· · ·	· · ·	· · ·	...
66	A10431+3514	HII	3	· · ·	· · ·	HII
67	A10448+0731	· · ·	· · ·	· · ·	· · ·	...
68	A10465+0711	HII	1	HII	1	HII
69	A10504+0454	HII	1	HII	1	HII
70	NGC 3454	HII	1	HII	3	HII
71	A10592+1652	HII	1	HII	1	HII
72	NGC 3499	· · ·	· · ·	· · ·	· · ·	...
73	NGC 3510	HII	1	HII	1	HII

TABLE 1 — *Continued*

ID	Name	Integrated		Nuclear		Adopted
		Class[a]	Quality[b]	Class[a]	Q[b]	Class[a]
74	A11017+3828W	…	…	…	…	...
75	NGC 3522	…	…	…	…	...
76	A11040+5130	HII	1	HII	3	HII
77	IC 673	HII	1	HII	1	HII
78	A11068+4705	…	…	…	…	...
79	A11072+1302	HII	1	HII	1	HII
80	NGC 3605	…	…	…	…	...
81	A11142+1804	HII	3	HII	1	HII
82	NGC 3633	HII	1	HII	1	HII
83	IC 692	AMB	1	AMB	1	AMB
84	A11238+5401	…	…	…	…	...
85	A11310+3254	HII	3	HII	1	HII
86	IC 708	…	…	…	…	...
87	A11332+3536	HII	1	HII	1	HII
88	A11336+5829	HII	1	HII	1	HII
89	NGC 3795A	HII	1	HII	3	HII
90	A11372+2012	HII	1	HII	1	HII
91	NGC 3795	HII	1	HII	3	HII
92	A11378+2840	HII	1	HII	1	HII
93	A11392+1615	HII	1	HII	1	HII
94	NGC 3846	HII	1	HII	1	HII
95	NGC 3850	…	…	…	…	...
96	A11476+4220	HII	1	HII	1	HII
97	NGC 3913	…	…	…	…	...
98	IC 746	HII	1	HII	1	HII
99	A11531+0132	…	…	…	…	...
100	NGC 3978	HII	1	HII	1	HII
101	A11547+4933	…	…	…	…	...
102	A11547+5813	HII	1	HII	1	HII
103	NGC 4034	HII	1	…	…	HII
104	A11592+6237	HII	1	HII	1	HII
105	A12001+6439	HII	1	HII	1	HII
106	NGC 4117	AMB	1	AMB	1	AMB
107	NGC 4120	HII	1	HII	1	HII
108	A12064+4201	HII	3	HII	1	HII
109	NGC 4141	HII	1	HII	1	HII
110	NGC 4159	HII	1	HII	1	HII
111	NGC 4204	…	…	…	…	...
112	NGC 4238	HII	1	HII	1	HII
113	NGC 4248	HII	1	HII	1	HII
114	A12167+4938	HII	1	HII	3	HII
115	NGC 4272	…	…	…	…	...
116	NGC 4288	HII	1	HII	1	HII
117	NGC 4308	…	…	…	…	...
118	A12195+3222	…	…	…	…	...
119	A12195+7535	Sy1	1	Sy1	1	AGN
120	A12263+4331	…	…	…	…	...
121	A12295+4007	HII	1	HII	1	HII
122	A12300+4259	HII	1	…	…	HII
123	A12304+3754	HII	1	HII	1	HII
124	NGC 4509	HII	1	HII	1	HII
125	A12331+7230	HII	1	HII	1	HII
126	A12446+5155	HII	1	HII	1	HII
127	NGC 4758	HII	1	HII	1	HII
128	NGC 4795	…	…	…	…	...
129	NGC 4807	…	…	…	…	...
130	NGC 4841B	…	…	…	…	...
131	NGC 4926	…	…	…	…	...
132	NGC 4961	…	…	…	…	...
133	A13065+5420	HII	1	HII	1	HII
134	IC 4213	HII	1	HII	1	HII
135	A13194+4232	HII	1	HII	3	HII
136	NGC 5117	…	…	…	…	...
137	NGC 5173	AMB	1	AMB	1	AMB
138	A13281+3153	…	…	…	…	...
139	NGC 5208	…	…	…	…	...
140	NGC 5230	HII	1	HII	3	HII
141	A13361+3323	HII	1	HII	1	HII
142	NGC 5267	…	…	…	…	...
143	A13422+3526	HII	1	HII	1	HII
144	NGC 5338	HII	3	HII	1	HII
145	NGC 5356	HII	3	HII	3	HII
146	A13550+4613	…	…	…	…	...
147	NGC 5407	…	…	…	…	...

TABLE 1 — *Continued*

ID	Name	Integrated		Nuclear		Adopted
		Class[a]	Quality[b]	Class[a]	Q[b]	Class[a]
148	NGC 5425	HII	1	HII	1	HII
149	A14016+3559	· · ·	· · ·	· · ·	· · ·	...
150	NGC 5470	· · ·	· · ·	· · ·	· · ·	...
151	NGC 5491	HII	3	· · ·	· · ·	HII
152	NGC 5532	· · ·	· · ·	· · ·	· · ·	...
153	NGC 5541	HII	1	· · ·	· · ·	HII
154	NGC 5596	· · ·	· · ·	· · ·	· · ·	...
155	NGC 5608	HII	1	HII	1	HII
156	A14305+1149	HII	1	HII	1	HII
157	NGC 5684	· · ·	· · ·	AGN	· · ·	AGN
158	NGC 5762	HII	1	· · ·	· · ·	HII
159	A14489+3547	HII	1	HII	1	HII
160	A14492+3545	HII	1	HII	1	HII
161	IC 1066	HII	1	· · ·	· · ·	HII
162	A14594+4454	AMB	1	AMB	1	AMB
163	A15016+1037	Sy1	1	Sy1	1	AGN
164	IC 1100	HII	3	HII	3	HII
165	NGC 5874	HII	1	HII	3	HII
166	NGC 5875A	HII	1	HII	1	HII
167	NGC 5888	· · ·	· · ·	· · ·	· · ·	...
168	IC 1124	HII	1	HII	3	HII
169	NGC 5940	Sy1	1	Sy1	1	AGN
170	A15314+6744	HII	1	HII	3	HII
171	NGC 5993	HII	1	HII	1	HII
172	IC 1141	AMB	1	AMB	1	AMB
173	IC 1144	· · ·	· · ·	· · ·	· · ·	...
174	NGC 6007	HII	1	· · ·	· · ·	HII
175	A15523+1645	HII	1	HII	1	HII
176	A15542+4800	· · ·	· · ·	· · ·	· · ·	...
177	NGC 6020	· · ·	· · ·	· · ·	· · ·	...
178	NGC 6123	· · ·	· · ·	· · ·	· · ·	...
179	NGC 6131	HII	1	HII	3	HII
180	NGC 6185	· · ·	· · ·	· · ·	· · ·	...
181	NGC 7077	HII	1	HII	1	HII
182	NGC 7194	· · ·	· · ·	· · ·	· · ·	...
183	A22306+0750	HII	1	HII	1	HII
184	NGC 7328	HII	3	HII	3	HII
185	NGC 7360	· · ·	· · ·	AMB	1	AMB
186	A22426+0610	HII	1	· · ·	· · ·	HII
187	A22551+1931N	HII	1	HII	1	HII
188	NGC 7436	· · ·	· · ·	· · ·	· · ·	...
189	NGC 7460	HII	1	HII	1	HII
190	NGC 7537	HII	1	HII	1	HII
191	NGC 7548	· · ·	· · ·	· · ·	· · ·	...
192	A23176+1541	HII	1	HII	3	HII
193	NGC 7620	HII	1	HII	3	HII
194	A23264+1703	· · ·	· · ·	· · ·	· · ·	...
195	IC 1504	HII	2	HII	3	HII
196	NGC 7752	HII	1	HII	1	HII
197	A23514+2813	· · ·	· · ·	· · ·	· · ·	...
198	A23542+1633	HII	1	HII	1	HII

[a] Classes 'HII', 'AMB' and 'AGN' are defined according to the Kewley et al. (2001b) theoretical classification scheme.

[b] Quality flags, Q, are defined as: 1= object classified using [NII]/Hα, [SII]/Hα, and [OIII]/Hβ; 2= object classified using [NII]/Hα and [OIII]/Hβ only; 3= object classified using [NII]/Hα only.

TABLE 2

Properties of the 101 galaxies selected from the NFGS

ID	Name	T	cz	M_B	μ_0^B	I/I_{B26}		ζ	log(O/H)+12		$A(V)$		SFR(Hα)	
						nuc	int		nuc	int	nuc	int	nuc	int
(1)	(2)	(3)	(4)	(5)	(6)	(7)	(8)	(9)	(10)	(11)	(12)	(13)	(14)	(15)
2	A00289+0556	7	2055	–17.84	20.64	0.058	0.919	0.063	8.82	8.71	< 0.02	0.93	0.006	0.259
4	A00389-0159	1	5302	–20.52	18.89	0.098	0.862	0.113	8.94	8.94	2.22	1.46	0.394	4.985
5	A00442+3224	3	4859	–20.31	20.17	0.039	0.771	0.051	9.08	8.92	1.99	1.23	0.286	3.191
15	A01300+1804	10	686	–15.90	20.46	0.058	0.869	0.067	8.06	8.06	0.50	0.50	0.001	0.022
16	A01344+2838	4	7756	–20.53	19.35	0.142	0.904	0.157	8.84	8.78	1.79	1.41	0.416	6.929
17	A01346+0438	4	3158	–18.40	19.85	0.188	0.957	0.197	8.85	8.77	0.81	0.98	0.142	0.802
19	NGC695	5	9705	–21.71	20.12	0.081	0.832	0.098	8.96	8.89	2.72	2.49	9.034	104.2
23	IC197	4	6332	–20.20	20.30	0.073	0.854	0.086	8.97	8.87	1.96	1.41	0.212	4.573
24	IC1776	5	3405	–19.27	21.58	0.019	0.903	0.021	8.77	8.54	0.04	0.62	0.008	0.908
25	A02056+1444	3	4405	–19.99	20.33	0.048	0.715	0.067	8.90	8.90	2.35	1.46	0.412	3.008
28	A02257-0134	8	1762	–17.76	21.66	0.020	0.522	0.038	9.05	8.72	0.33	0.78	0.002	0.119
34	A03202-0205	1	8227	–20.92	19.68	0.099	0.860	0.115	9.10	8.93	1.13	1.35	0.330	5.445
38	A09045+3328	8	553	–15.20	21.68	0.025	0.662	0.037	7.94	8.67	< 0.02	0.13	0.0001	0.005
39	NGC2780	2	1951	–17.91	21.05	0.037	0.795	0.046	9.11	9.03	1.20	1.12	0.024	0.154
41	NGC2799	9	1882	–18.13	20.11	0.094	0.815	0.115	8.96	8.84	0.47	0.97	0.050	0.315
43	NGC2844	1	1486	–18.18	19.17	0.091	0.864	0.106	8.68	8.81	2.47	1.22	0.026	0.166
45	NGC3009	5	4666	–19.50	19.92	0.073	0.787	0.092	9.23	8.93	1.43	1.00	0.100	0.828
46	IC2520	...	1226	–17.53	19.88	0.068	0.719	0.094	8.91	8.84	1.42	1.51	0.028	0.574
47	A09557+4758	9	1172	–17.90	21.40	0.018	0.780	0.024	7.90	8.51	0.17	0.12	0.001	0.125
48	NGC3075	5	3566	–19.49	20.09	0.055	0.794	0.069	9.13	8.97	0.96	0.49	0.175	0.795
49	A09579+0439	3	4185	–19.14	20.75	0.072	0.918	0.078	9.01	8.76	1.29	1.52	0.065	1.491
51	A10042+4716	10	571	–15.88	21.85	0.017	0.762	0.022	8.72	8.67	0.02	0.18	0.0001	0.012
55	A10171+3853	9	2008	–18.10	21.04	0.034	0.761	0.044	8.79	8.85	0.54	0.27	0.004	0.130
56	NGC3213	4	1412	–17.90	20.58	0.035	0.791	0.045	8.88	8.81	< 0.02	1.32	0.0004	0.120
57	NGC3264	8	929	–17.58	21.41	0.016	0.788	0.020	8.65	8.62	< 0.02	< 0.02	0.002	0.118
58	NGC3279	5	1422	–18.04	20.92	0.020	0.866	0.023	9.02	8.89	1.24	1.81	0.005	0.300
59	A10321+4649	5	3338	–18.91	19.31	0.150	0.782	0.192	9.07	9.06	1.09	0.97	0.181	0.717
60	A10337+1358	6	2997	–18.83	20.92	0.035	0.756	0.046	8.91	8.89	2.03	1.43	0.050	0.974
61	IC2591	4	6755	–20.49	19.62	0.107	0.877	0.122	8.98	8.79	0.88	0.67	0.290	3.077
62	A10365+4812	5	854	–16.34	20.07	0.089	0.713	0.124	8.14	8.06	0.10	< 0.02	0.002	0.018
63	A10368+4811	5	1534	–17.41	20.86	0.066	0.794	0.083	8.22	8.35	0.49	0.41	0.004	0.090
64	NGC3326	3	8136	–20.78	18.65	0.215	0.815	0.263	9.09	8.98	2.44	1.89	3.126	8.130
68	A10465+0711	0	722	–14.92	20.10	0.101	0.776	0.130	8.63	8.26	0.37	0.44	0.002	0.012
69	A10504+0454	0	5793	–19.97	18.14	0.334	0.882	0.378	8.92	8.91	0.91	0.73	1.990	2.617
70	NGC3454	5	1153	–17.37	21.50	0.020	0.843	0.024	8.81	8.79	1.43	0.76	0.003	0.113
71	A10592+1652	4	2936	–18.44	21.29	0.045	0.738	0.062	8.77	8.57	0.06	0.48	0.007	0.241
73	NGC3510	7	704	–16.39	20.69	0.028	0.859	0.032	8.65	8.59	0.06	0.15	0.001	0.081
76	A11040+5130	5	2204	–19.25	21.13	0.014	0.677	0.021	8.79	8.74	< 0.02	0.20	0.002	0.276
77	IC673	1	3851	–19.45	20.14	0.079	0.815	0.097	9.05	8.96	1.76	1.24	0.163	1.355
79	A11072+1302	5	12743	–21.38	20.29	0.133	0.898	0.148	8.93	8.79	1.15	1.00	1.937	16.24
81	A11142+1804	5	973	–16.04	21.32	0.033	0.763	0.044	9.03	8.87	1.44	1.80	0.003	0.074
82	NGC3633	1	2553	–18.92	19.66	0.109	0.877	0.124	9.15	8.91	2.34	2.73	0.252	2.226
85	A11310+3254	3	2619	–18.69	20.36	0.059	0.715	0.082	9.03	8.69	1.38	1.79	0.012	0.253
87	A11332+3536	–3	1598	–17.89	18.75	0.190	0.847	0.225	8.82	8.78	1.33	0.80	0.106	0.134
88	A11336+5829	5	1225	–17.45	21.28	0.032	0.541	0.058	8.34	8.54	< 0.02	0.37	0.002	0.049
89	NGC3795A	6	1154	–18.03	21.89	0.010	0.780	0.012	8.75	8.62	2.88	< 0.02	0.001	0.059
90	A11372+2012	5	10964	–21.60	19.79	0.097	0.875	0.111	9.27	8.92	1.29	0.92	0.480	13.13
91	NGC3795	5	1091	–17.48	20.71	0.020	0.796	0.025	8.95	8.72	0.52	0.90	0.0005	0.057
92	A11378+2840	–3	1821	–17.59	19.94	0.164	0.886	0.184	8.65	8.61	0.33	0.49	0.015	0.104
93	A11392+1615	–2	786	–14.82	19.80	0.171	0.752	0.228	8.63	8.62	0.17	0.18	0.009	0.026
94	NGC3846	9	1396	–18.22	20.92	0.023	0.825	0.028	8.71	8.66	0.20	< 0.02	0.002	0.135
96	A11476+4220	–2	1033	–16.62	19.26	0.254	0.794	0.320	8.94	8.91	0.54	0.74	0.030	0.068
98	IC746	3	5027	–19.59	20.11	0.103	0.830	0.124	8.89	8.66	0.53	0.98	0.065	1.458
100	NGC3978	4	9978	–22.22	20.23	0.037	0.877	0.043	9.29	9.02	1.17	1.28	0.447	25.74
102	A11547+5813	9	1175	–17.06	21.91	0.025	0.842	0.029	8.19	8.17	0.72	0.22	0.001	0.042
104	A11592+6237	10	1120	–17.08	21.44	0.033	0.828	0.039	8.37	8.27	< 0.02	< 0.02	0.005	0.049
105	A12001+6439	–2	1447	–17.62	18.50	0.242	0.906	0.268	8.89	8.83	1.00	1.02	0.157	0.409
107	NGC4120	5	2251	–18.61	21.12	0.038	0.748	0.050	8.71	8.69	0.69	0.46	0.015	0.332
108	A12064+4201	2	927	–17.05	20.32	0.063	0.790	0.080	9.09	8.98	1.31	1.37	0.019	0.076
109	NGC4141	5	1980	–19.08	20.54	0.035	0.857	0.041	8.74	8.60	< 0.02	0.23	0.007	0.565
110	NGC4159	8	1761	–18.13	20.63	0.047	0.866	0.054	8.72	8.64	0.66	0.94	0.010	0.369
112	NGC4238	5	2771	–18.96	21.10	0.036	0.782	0.046	8.87	8.75	0.42	0.45	0.034	0.586
113	NGC4248	8	484	–16.31	21.32	0.013	0.808	0.015	8.27	8.70	2.28	1.01	0.001	0.023
114	A12167+4938	5	3639	–19.38	20.85	0.036	0.801	0.045	9.05	8.74	0.64	1.07	0.023	0.912
116	NGC4288	9	532	–16.40	20.46	0.023	0.839	0.028	8.71	8.52	< 0.02	0.41	0.001	0.044
121	A12295+4007	7	685	–16.04	20.97	0.037	0.885	0.042	8.25	7.93	< 0.02	< 0.02	0.001	0.021
123	A12304+3754	7	503	–16.07	21.02	0.014	0.791	0.018	8.64	8.65	< 0.02	0.07	0.0004	0.023
124	NGC4509	9	907	–16.73	20.57	0.066	0.845	0.078	8.25	8.21	< 0.02	0.11	0.019	0.095
125	A12331+7230	3	6959	–20.38	20.29	0.075	0.773	0.097	8.99	8.85	1.09	1.43	0.298	5.127
126	A12446+5155	10	502	–16.48	20.75	0.028	0.786	0.035	8.04	7.88	< 0.02	< 0.02	0.001	0.012
127	NGC4758	4	1244	–18.35	21.46	0.011	0.762	0.014	8.30	8.62	2.56	1.29	0.008	0.225
133	A13065+5420	3	2460	–18.46	21.10	0.040	0.798	0.050	8.74	8.52	0.34	0.21	0.008	0.308
134	IC4213	6	815	–16.74	21.43	0.022	0.834	0.026	8.63	8.57	< 0.02	0.38	0.001	0.041

TABLE 2 — *Continued*

ID	Name	T	cz	M_B	μ_0^B	I/I_{B26}		ζ	log(O/H)+12		$A(V)$		SFR(Hα)	
						nuc	int		nuc	int	nuc	int	nuc	int
(1)	(2)	(3)	(4)	(5)	(6)	(7)	(8)	(9)	(10)	(11)	(12)	(13)	(14)	(15)
135	A13194+4232	6	3396	–19.03	20.48	0.056	0.800	0.070	8.95	8.83	0.84	0.88	0.039	0.643
141	A13361+3323	9	2364	–18.53	21.52	0.019	0.668	0.029	8.61	8.36	0.26	0.53	0.011	0.331
143	A13422+3526	4	2502	–18.38	20.74	0.060	0.784	0.076	8.81	8.70	1.03	1.02	0.013	0.226
145	NGC5356	3	1397	–18.71	21.02	0.016	0.760	0.021	9.08	8.67	1.05	3.29	0.002	0.929
148	NGC5425	5	2062	–18.48	21.00	0.035	0.792	0.044	8.93	8.76	0.97	0.78	0.008	0.276
153	NGC5541	5	7698	–21.29	19.86	0.071	0.903	0.079	8.96	8.94	1.22	1.47	0.253	12.53
155	NGC5608	9	662	–16.48	22.04	0.015	0.861	0.017	7.96	8.03	< 0.02	< 0.02	0.0001	0.014
156	A14305+1149	5	2234	–18.61	20.84	0.036	0.898	0.040	8.90	8.77	0.53	0.39	0.005	0.268
159	A14489+3547	...	1215	–16.94	18.85	0.323	0.866	0.373	8.26	8.24	< 0.02	< 0.02	0.069	0.167
160	A14492+3545	...	1306	–17.35	20.08	0.092	0.863	0.106	8.55	8.24	0.09	0.28	0.005	0.066
161	IC1066	2	1613	–18.31	20.01	0.061	0.907	0.068	8.95	8.72	0.46	1.53	0.001	0.308
164	IC1100	6	6561	–20.71	19.67	0.086	0.834	0.103	9.17	9.00	0.83	1.57	0.154	4.428
165	NGC5874	4	3128	–19.83	21.24	0.014	0.792	0.018	8.79	8.80	< 0.02	1.60	0.002	1.066
166	NGC5875A	5	2470	–18.52	20.47	0.068	0.642	0.106	8.91	8.92	0.57	0.40	0.028	0.256
168	IC1124	2	5242	–19.86	19.79	0.094	0.871	0.108	8.93	8.97	2.69	1.99	0.347	3.223
170	A15314+6744	5	6461	–20.49	20.54	0.037	0.868	0.042	9.30	8.99	0.51	0.70	0.028	1.841
171	NGC5993	3	9578	–21.65	19.88	0.060	0.826	0.073	9.09	9.02	0.72	0.83	0.198	8.109
175	A15523+1645	5	2191	–17.84	20.12	0.142	0.820	0.173	8.79	8.62	0.27	0.84	0.029	0.289
179	NGC6131	5	5054	–20.46	20.97	0.029	0.795	0.036	9.11	8.99	0.92	0.41	0.076	1.113
181	NGC7077	0	1142	–16.88	19.38	0.167	0.823	0.203	8.65	8.54	0.34	0.48	0.016	0.097
183	A22306+0750	5	1995	–18.05	20.17	0.082	0.801	0.102	8.91	8.87	2.13	1.75	0.077	0.864
187	A22551+1931N	–2	5682	–18.84	19.93	0.264	0.740	0.357	8.90	8.90	1.82	1.90	2.002	4.014
189	NGC7460	3	3296	–19.92	20.01	0.031	0.728	0.042	9.17	8.97	1.99	1.47	0.263	3.124
190	NGC7537	4	2648	–19.10	19.77	0.059	0.819	0.072	9.04	8.93	0.66	1.28	0.037	1.874
193	NGC7620	6	9565	–21.87	18.75	0.108	0.913	0.118	8.96	8.88	2.12	1.74	2.280	38.98
195	IC1504	3	6306	–20.56	20.67	0.041	0.797	0.051	9.18	8.78	2.47	2.84	0.464	14.86
196	NGC7752	7	4902	–19.70	19.90	0.130	0.730	0.179	8.95	8.97	1.61	1.14	2.015	5.433
198	A23542+1633	10	1788	–17.83	21.43	0.022	0.813	0.027	8.71	8.08	0.09	0.35	0.005	0.282

TABLE 3
Relative B_{26} covering fraction ζ, metallicity ratio, A(V) and SFR as a function of galaxy type.

Hubble	#	z	Diam	ζ		Δlog(O/H)		ΔA(V)		ΔSFR	
Type		mean[a]	(kpc)	mean[a]	rms	mean[ab]	rms[c]	mean[ad]	rms[e]	mean[a]	rms
S0-Sab	18	0.0101	13.38	0.18 ± 0.02	0.10	0.09 ± 0.03	0.12	0.13 ± 0.13	0.50	1.47 ± 0.23	0.94
Sb-Sd	61	0.0139	19.87	0.07 ± 0.01	0.05	0.14 ± 0.02	0.13	0.07 ± 0.10	0.69	0.85 ± 0.08	0.63
Sdm-Im-Pec	22	0.0048	8.38	0.06 ± 0.01	0.08	0.11 ± 0.06	0.30	-0.001 ± 0.09	0.36	0.96 ± 0.13	0.61

[a] The error quoted is the standard error of the mean

[b] The mean of Δlog(O/H) is the logarithm of the arithmetic mean of the (O/H) values

[c] The rms of Δlog(O/H) is calculated in log(O/H) units using the mean in *b*

[d] The mean of ΔA(V) is calculated by taking the mean Balmer Decrement and converting to A(V) assuming case b recombination and $R_V = A_V/E(B-V) = 3.1$

[e] The rms of Δlog(O/H) is calculated in A(V) units using the mean in *d*

TABLE 4
Mean elliptical radii at various relative and absolute fractions of the B_{26} light

ζ	$I_{B_{26}}$	mean elliptical radius (arcsec)			
		All mean±error(rms)	S0-Sab mean±error(rms)	Sb-Sd mean±error(rms)	Sdm-Im/Pec mean±error(rms)
10%	8.1%	3.51±0.02(1.68)	2.04±0.01(0.85)	3.64±0.02(1.63)	4.34±0.02(1.63)
···	10.0%	3.99±0.02(1.92)	2.33±0.01(0.99)	4.15±0.02(1.88)	4.92±0.02(1.86)
20%	16.2%	5.44±0.03(2.64)	3.23±0.01(1.38)	5.65±0.03(2.60)	6.67±0.04(2.57)
···	20.0%	6.25±0.03(3.04)	3.75±0.02(1.59)	6.49±0.03(3.00)	7.67±0.04(2.95)
30%	24.3%	7.15±0.04(3.48)	4.31±0.02(1.82)	7.39±0.04(3.43)	8.78±0.05(3.39)
···	30.0%	8.31±0.05(4.04)	5.07±0.02(2.10)	8.57±0.05(3.98)	10.25±0.07(3.97)
40%	32.4%	8.80±0.05(4.27)	5.39±0.02(2.22)	9.06±0.05(4.21)	10.87±0.07(4.21)
···	40.0%	10.36±0.07(4.99)	6.48±0.03(2.60)	10.61±0.07(4.90)	12.86±0.10(4.98)
50%	40.5%	10.47±0.07(5.04)	6.55±0.03(2.62)	10.71±0.07(4.95)	12.99±0.10(5.03)
60%	48.6%	12.22±0.09(5.80)	7.87±0.05(3.08)	12.43±0.09(5.67)	15.21±0.13(5.88)
···	50.0%	12.54±0.09(5.93)	8.11±0.05(3.16)	12.74±0.09(5.80)	15.61±0.14(6.04)
70%	56.7%	14.15±0.12(6.60)	9.42±0.07(3.64)	14.28±0.12(6.43)	17.64±0.19(6.84)
···	60.0%	15.00±0.14(6.96)	10.14±0.08(3.91)	15.09±0.13(6.76)	18.73±0.22(7.30)
80%	64.8%	16.32±0.17(7.51)	11.32±0.10(4.39)	16.33±0.16(7.25)	20.39±0.27(8.01)
···	70.0%	17.88±0.22(8.14)	12.76±0.13(4.99)	17.79±0.20(7.80)	22.33±0.34(8.84)
90%	72.9%	18.83±0.25(8.50)	13.63±0.15(5.31)	18.69±0.23(8.12)	23.49±0.39(9.33)
···	80.0%	21.51±0.37(9.45)	16.18±0.25(6.22)	21.19±0.34(8.93)	26.73±0.56(10.64)
100%	81.0%	21.94±0.40(9.60)	16.61±0.27(6.38)	21.60±0.37(9.05)	27.24±0.59(10.84)
···	90.0%	26.94±0.80(11.05)	21.63±0.56(8.12)	26.32±0.75(10.29)	33.00±1.14(12.70)
···	100.0%	39.57±3.63(12.91)	33.75±3.30(9.75)	38.98±3.61(12.17)	45.99±3.98(14.82)

TABLE 5
Fraction of galaxy type in each luminosity range shown in Figure 1.

Hubble	# of	Fraction of galaxies within each M_B bin[a]		
Type	galaxies	$-18.12 < M_B$	$-20.22 < M_B \leq -18.12$	$M_B \leq -20.22$
S0-Sab	18	0.50	0.39	0.11
Sb-Sd	61	0.26	0.48	0.26
Sdm-Im-Pec	22	0.82	0.18	0.00

[a] We assume $M_* = -20.22$ (Marzke et al. 1998, ; after conversion to our adopted cosmology).